Article

Developmental Cell

Deceleration of the cell cycle underpins a switch from proliferative to terminal divisions in plant stomatal lineage

Graphical abstract

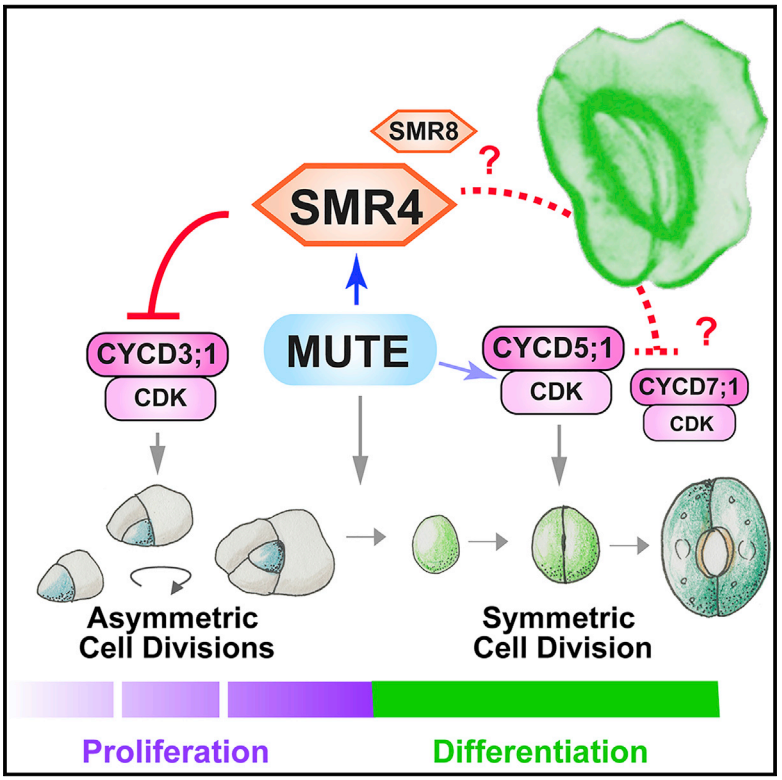

Highlights

- During stomatal differentiation, asymmetric divisions are faster than terminal divisions
- Upon commitment to differentiation, MUTE induces the cell-cycle inhibitor SMR4
- SMR4 decelerates the asymmetric cell division cycle via selective binding to cyclin D
- Regulating duration of the G1 phase is critical for epidermal cell fate specification

Authors

Soon-Ki Han, Arvid Herrmann, Jiyuan Yang, ..., Crisanto Gutierrez, Eun-Deok Kim, Keiko U. Torii

Correspondence

ktorii@utexas.edu

In brief

Stomata, which are cellular valves in the plant epidermis, differentiate via fast asymmetric divisions of a precursor, followed by a single slower symmetric division. Han et al. identify a plant-specific, cyclin-dependent kinase inhibitor that regulates the length of cell cycles in the stomatal lineage to enable the transition from proliferation to differentiation.

Han et al., 2022, Developmental Cell *57*, 569–582
March 14, 2022
https://doi.org/10.1016/j.devcel.2022.01.014

CellPress

Developmental Cell

CellPress
OPEN ACCESS

Article

Deceleration of the cell cycle underpins a switch from proliferative to terminal divisions in plant stomatal lineage

Soon-Ki Han,[1,2,7] Arvid Herrmann,[3,4] Jiyuan Yang,[4] Rie Iwasaki,[1] Tomoaki Sakamoto,[5] Bénédicte Desvoyes,[6] Seisuke Kimura,[5] Crisanto Gutierrez,[6] Eun-Deok Kim,[3,4] and Keiko U. Torii[1,3,4,8,*]

[1]Institute of Transformative Bio-Molecules (WPI-ITbM), Nagoya University, Nagoya, Aichi 464-8601, Japan
[2]Institute for Advanced Research (IAR), Nagoya University, Nagoya, Aichi 464-8601, Japan
[3]Howard Hughes Medical Institute, The University of Texas at Austin, Austin, TX 78712, USA
[4]Department of Molecular Biosciences, The University of Texas at Austin, Austin, TX 78712, USA
[5]Department of Industrial Life Sciences and Center for Plant Sciences, Kyoto Sangyo University, Kyoto-shi, Kyoto 603-8555, Japan
[6]Centro de Biologia Molecular Severo Ochoa, Nicolas Cabrera 1, Cantoblanco, 28049 Madrid, Spain
[7]Present address: Department of New Biology, DGIST (Daegu Gyeongbuk Institute of Science and Technology), Daegu 42988, Republic of Korea
[8]Lead contact
*Correspondence: ktorii@utexas.edu
https://doi.org/10.1016/j.devcel.2022.01.014

SUMMARY

Differentiation of specialized cell types requires precise cell-cycle control. Plant stomata are generated through asymmetric divisions of a stem-cell-like precursor followed by a single symmetric division that creates paired guard cells surrounding a pore. The stomatal-lineage-specific transcription factor MUTE terminates the asymmetric divisions and commits to differentiation. However, the role of cell-cycle machineries in this transition remains unknown. We discover that the symmetric division is slower than the asymmetric division in Arabidopsis. We identify a plant-specific cyclin-dependent kinase inhibitor, SIAMESE-RELATED4 (SMR4), as a MUTE-induced molecular brake that decelerates the cell cycle. SMR4 physically and functionally associates with CYCD3;1 and extends the G1 phase of asymmetric divisions. By contrast, SMR4 fails to interact with CYCD5;1, a MUTE-induced G1 cyclin, and permits the symmetric division. Our work unravels a molecular framework of the proliferation-to-differentiation switch within the stomatal lineage and suggests that a timely proliferative cell cycle is critical for stomatal-lineage identity.

INTRODUCTION

Growth and development of multicellular organisms rely on faithful cell-cycle progression, in which fundamental mechanism is highly conserved across the eukaryote kingdoms (Elledge, 1996; Harashima et al., 2013). Accumulating evidence in metazoans emphasizes that cell-cycle machinery is modulated during development, operating distinctly in proliferating stem cells versus differentiating cells (Budirahardja and Gönczy, 2009). For example, early embryogenesis of flies, fish, and frogs, as well as murine embryonic stem cells, execute rapid cell-cycle mode due to shortened gap phases. As they undergo fate specification or differentiation, the duration of cell-cycle increases (Coronado et al., 2013; Dalton, 2015; Liu et al., 2019).

A typical eukaryotic cell cycle is composed of four distinct phases, G1-S-G2-M. Cell-cycle progression is driven by the oscillation of cyclin-dependent kinase (CDK) activity triggered by phase-specific cyclins, which are tightly regulated by the level of synthesis and proteolysis (Harashima et al., 2013; Morgan, 2007). CDK activity is negatively regulated by cyclin-dependent kinase inhibitors (CKIs). The G1/S transition is initiated by D-type cyclin (CyclinD) and CDK complex, which relieve retinoblastoma (Rb)-mediated repression on S phase gene expression (Bertoli et al., 2013; Desvoyes and Gutierrez, 2020). Accumulating studies suggest that the G1 extension is indicative of differentiation (Coronado et al., 2013; Liu et al., 2019).

Plants possess a large number of genes encoding cyclins, CDKs, and CKIs (Inzé and De Veylder, 2006). Studies have shown how specific cell-cycle components are coupled to developmental patterning. For example, during Arabidopsis root development, transcription factors SHORTROOT and SCARECROW directly induce a CyclinD, CYCD6;1, that drives a formative cell division to create root endodermis and cortex cells (Sozzani et al., 2010). Another example is lateral root formation, in which auxin-induced formative division is modulated by CYCD2;1 and plant CKI, KIP-RELATED PROTEIN2 (KRP2, also known as ICK2) (Sanz et al., 2011). Some highly specialized plant cell types, such as epidermal pavement cells and trichomes,

undergo endoreduplication at the onset of terminal differentiation (Inzé and De Veylder, 2006). Plant-specific CKIs, including SIAMESE (SIM) and SIAMESE-RELATED1 (SMR1, also known as LGO) regulate morphogenesis of trichomes and sepal giant cells, respectively, by promoting endoreduplication presumably via inhibiting CDK activity (Hamdoun et al., 2016; Roeder et al., 2010; Walker et al., 2000). It remains unclear if the modulation of cell cycle contributes to switching the cell division mode—from stem cell divisions to differentiating cell divisions—in plants.

Development of stomata, valves on the plant aerial epidermis for gas exchange and water control, is an accessible model of *de novo* initiation and differentiation of lineage-specific stem cells. In Arabidopsis, birth of pores begins with the stomatal lineage fate specification of protodermal cells, which forms bipotent meristemoid mother cells (MMC) able to become either stomata or pavement cells (Han and Torii, 2016; Lau and Bergmann, 2012). A series of asymmetric cell division (ACD) follows to amplify the number of stomatal lineage precursor cells: meristemoids and stomatal lineage ground cells (SLGCs). The meristemoid renews itself after ACD, thus behaving as a transient stem cell. After a few rounds of ACDs, a single round of terminal symmetric cell division (SCD) of a guard mother cell (GMC) proceeds, completing a stoma composed of paired guard cells (Han and Torii, 2016; Lau and Bergmann, 2012) (Figure 1A).

Accumulating evidence supports that master-regulatory bHLH proteins SPEECHLESS (SPCH), MUTE, and FAMA govern cell-state transitions within the stomatal lineage, in part via directly regulating the expression of cell-cycle genes (Adrian et al., 2015; Hachez et al., 2011; Han et al., 2018; Lau et al., 2014) (Figure 1A). SPCH initiates and sustains the ACDs of a meristemoid in part via upregulating CyclinDs CYCD3;1 and 3;2 (MacAlister et al., 2007; Vatén et al., 2018). MUTE terminates proliferative cell state and drives final SCD by activating a large subset of cell-cycle regulators, including CYCD5;1 (Han et al., 2018; Pillitteri et al., 2007). FAMA and a Myb protein, FOUR LIPS, are directly induced by MUTE and inhibit SCD via direct suppression of the cell-cycle genes, thereby ensuring that the SCD occurs just once (Hachez et al., 2011; Han et al., 2018; Xie et al., 2010). However, it is not known how proliferative ACD switches to terminal SCD, and whether the core cell-cycle machinery contributes to this process.

Through time-lapse imaging of stomatal development using plant cell-cycle marker, Plant Cell-Cycle Indicator (PlaCCI) (Desvoyes et al., 2020), we discovered that the stomatal SCD cycle is slower than that of ACDs. Subsequent transcriptomic and ChIP-sequencing analyses identified that MUTE directly induces the expression of *SMR4* during meristemoid-to-GMC transition. Through loss-of-function and stomatal-lineage-specific overexpression of SMR4 as well as its functional interaction studies with CyclinDs, we elucidate that SMR4 acts as a molecular brake to decelerate cell cycle in G1 phase to ensure termination of the ACD cycle and facilitate faithful progression to SCD. Slowing down the ACD cycle resulted in skewed stomata with pavement cell-like characters. Taken together, we reveal a molecular framework of the cell proliferation-to-differentiation switch within the stomatal lineage and suggest that a timely proliferative ACD cycle is critical for the generation of stomata with proper GC size, shape, and identity.

RESULTS

The single symmetric division of stomatal precursor is slower than amplifying asymmetric division

The stomatal precursor cells execute a unique transition from amplifying ACD to a single SCD, a step coordinated by the bHLH protein MUTE (Figure 1A). To understand if a switch from the ACD-to-SCD division mode links to the cell-cycle dynamics, we first performed time-lapse imaging of developing cotyledon epidermis by using the multi-color PlaCCI (Desvoyes et al., 2020) (Figure 1C) and examined each phase of cell cycle during asymmetric and symmetric divisions (Figures 1B, 1D, and 1E; Video S1). The average cell-cycle time of ACD of meristemoid and SCD of GMC was 12 ± 1.64 and 20.27 ± 3.73 h, respectively (Figure 1B; Table S1), indicating that ACD is faster by ~7.5 h than SCD that creates a pair of guard cells. Measuring cell division time using a plasma-membrane GFP marker LTI6b (Kurup et al., 2005) yielded essentially the same results (Figure S1). On the basis of these findings, we conclude that the switching from ACD to SCD involves cell-cycle slow down.

SMR4 is expressed in stomatal lineage cells and directly induced by MUTE

In eukaryotic cells, CKIs negatively regulate cell-cycle progression. To identify a factor that plays a role in the decelerating cell cycle during the ACD-to-SCD transition, we surveyed publicly available transcriptome data (Han et al., 2018; Lau et al., 2014) to search for *CKIs* that are induced by SPCH and MUTE. Among the 7 *KRP* and 17 *SIM/SMR* genes (Kumar and Larkin, 2017; Peres et al., 2007), only *SMR4* exhibits marked increase by the induced *MUTE* overexpression (*iMUTE*) (Figure 2A). On the other hand, a majority of *SMRs* and *KRPs* is either downregulated or unchanged upon *iMUTE* or *iSPCH* (Figure 2A). Subsequently, we performed time course induction analysis. Consistent with the transcriptome data, *SMR4* expression was increased by iMUTE with similar kinetics to a known direct MUTE target, *TMM* (Han et al., 2018) (Figure 2B). In addition, iMUTE (and in a lesser extent, iSPCH) weakly induced *SMR8* (Figure S2).

Our previous transcriptome study (Han et al., 2018) found that MUTE induces a suite of cell-cycle- and mitotic-division-related genes driving the SCD of stomata. To test whether these genes are indeed direct MUTE targets, we performed genome-wide MUTE ChIP-sequencing (see STAR Methods) (Table S2). MUTE-bound genes as well as those MUTE-bound genes that are induced by MUTE are highly enriched in the Gene Ontology (GO) categories (Figure 2C; Table S2): "mitotic cell-cycle phase (83.22-fold enrichment, p = 2.15e-02)," "ACD (18.91-fold enrichment, p = 2.4e-02)" and other cell-cycle/mitosis-related categories (Figure 2C, pink bars), as well as the genes involved in stomatal development: "GMC differentiation (37.83-fold enrichment, p=8.34e-04)" and "stomatal complex development (22.7-fold enrichment, p = 1.75e-12)" (Figure 2C, cyan bars). Strong MUTE-bound peaks are detected at the 5′- and 3′- regions of known MUTE target loci, *ERL1*, *TMM*, *EPF2*, and *CDKB1;1* (Figure 2D). Most importantly, MUTE robustly bound to the 5′ region of *SMR4*, indicating that *SMR4* is a direct MUTE target. As expected, no MUTE binding peak was detected in *SMR1* loci,

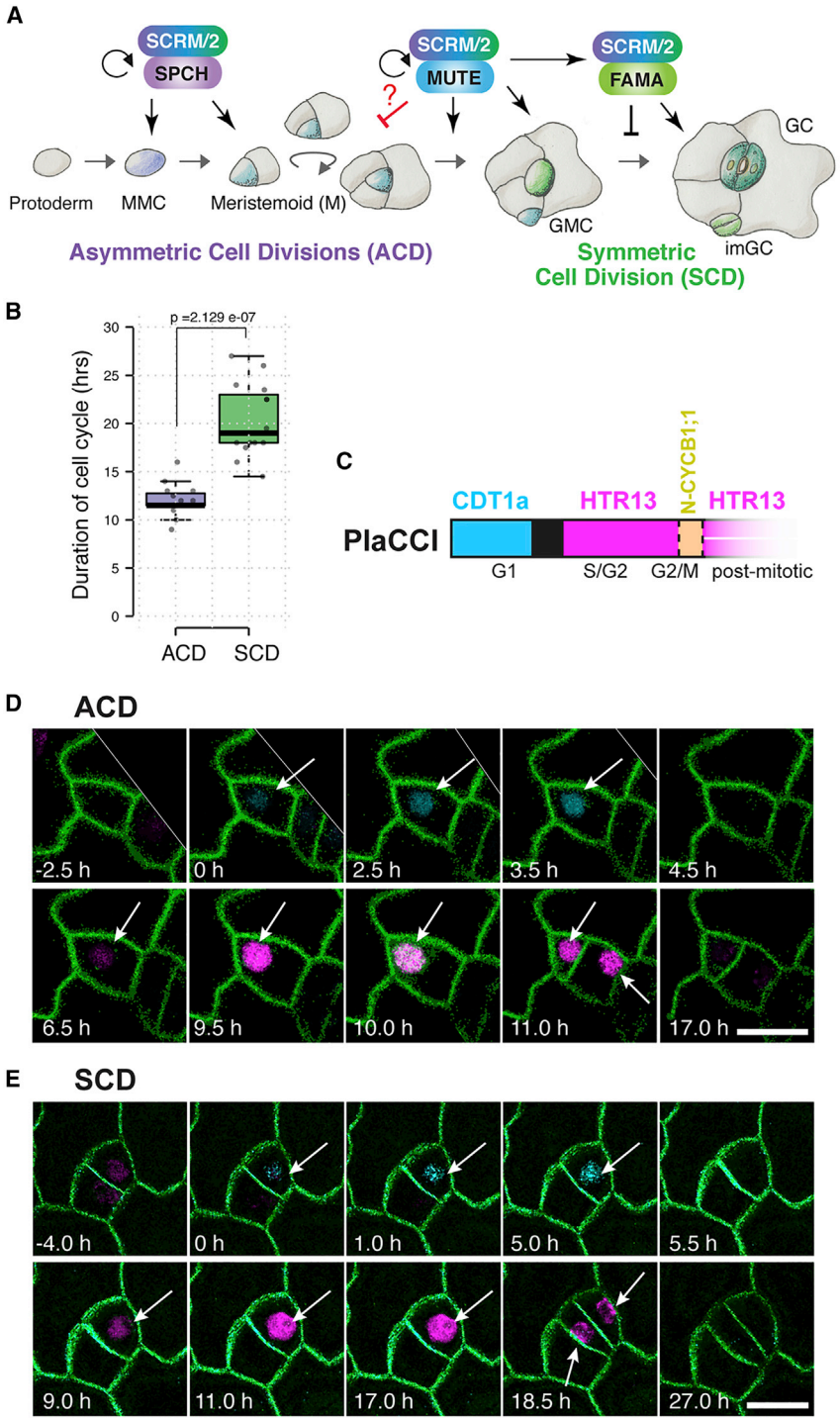

Figure 1. Cell-cycle duration between asymmetric cell division and symmetric cell division during stomatal development

(A) Cartoon of the heterodimeric transcription factors specifying stomatal development. A series of ACD is triggered by SPCH·SCRM/2 and a single symmetric cell division (SCD) is coordinated by MUTE·SCRM/2 and FAMA·SCRM/2. How the mode of cell cycle switches from ACD to SCD is not known (red line and question mark). MMC, meristemoid mother cell; M, meristemoid; GMC, guard mother cell; imGC and GC, immature and mature guard cell.

(B) Duration of the cell-cycle time of stomatal precursors undergoing ACD and SCD in wild type. n = 15 for each cell division mode. Two-tailed Student t test was performed. p = 2.129e^{-07}.

(C) PlaCCI color code. Cyan: CDT1a-CFP signal, onset of G1 phase; black: short period with no fluorescence signal; magenta: HTR13-mCherry signal, S/G2 through late M; orange: CYCB1;1-YFP signal. Postmitotic referred to G1 or G0 (terminal state).

(D and E) Representative time-lapse confocal images of ACD (D) and SCD (E) in stomatal lineage cells from 1- to 3-day-old cotyledon of Col-0 expressing both PlaCCI and LTi6B (green). CDT1a-CFP signal (cyan) marks the starting point (0 h) at the onset of G1 phase for ACD and SCD. Note that the CYCB1;1-YFP (D, green nucleus/chromosomes, M phase) is not always visible due to time-lapse recordings obtained at 30 min time intervals. Arrows point to nuclei with a fluorescent signal in different cell stages. Scale bar, 10 μm. See also Figure S1 and Table S1.

which is not induced by iMUTE and thus not a direct MUTE target (Figures 2B and 2D).

We further characterized the *SMR4* expression patterns using seedlings expressing nuclear-localized GFP driven by the *SMR4* promoter (*proSMR4*::*nucGFP*; Figure 2E). A strong GFP signal was detected in stomatal lineage cells, with the highest expression in a late meristemoid to GMC and persisted in immature GCs (Figure 2E). Likewise, a translational reporter of SMR4-YFP fusion protein driven by the *SMR4* promoter (*proSMR4*::*SMR4-YFP*) exhibited similar accumulation patterns predominantly in the nuclei (Figure 2F, arrows). A weak SMR4-YFP signal was also detected in the cytoplasm (Figure 2F, asterisks), which may imply the regulation of SMR4 proteins. These expression patterns mirror that of MUTE (Pillitteri et al., 2007). Finally, to address whether *MUTE* is required for the *SMR4* expression during the meristemoid-to-GMC transition, we examined the *SMR4* reporters in the *MUTE*-null mutant, *mute-2* (Pillitteri et al., 2008) (Figure S3). SMR4-YFP was not detected in the arrested *mute-2* meristemoids, and transcriptional reporter *proSMR4*::*nucGFP* signals were diminished (Figure S3). Combined, our results indicate that MUTE directly promotes the *SMR4* expression in stomatal precursor cells before the onset of the SCD and that MUTE is both necessary and sufficient for this boosted expression. We also noted weak, background-level of nucGFP signals in few meristemoids (Figure S3B), implying a putative role for SMR4 in a *MUTE* independent process. The *SMR4* expression suggests its distinct role from that of canonical CKIs in endorduplication.

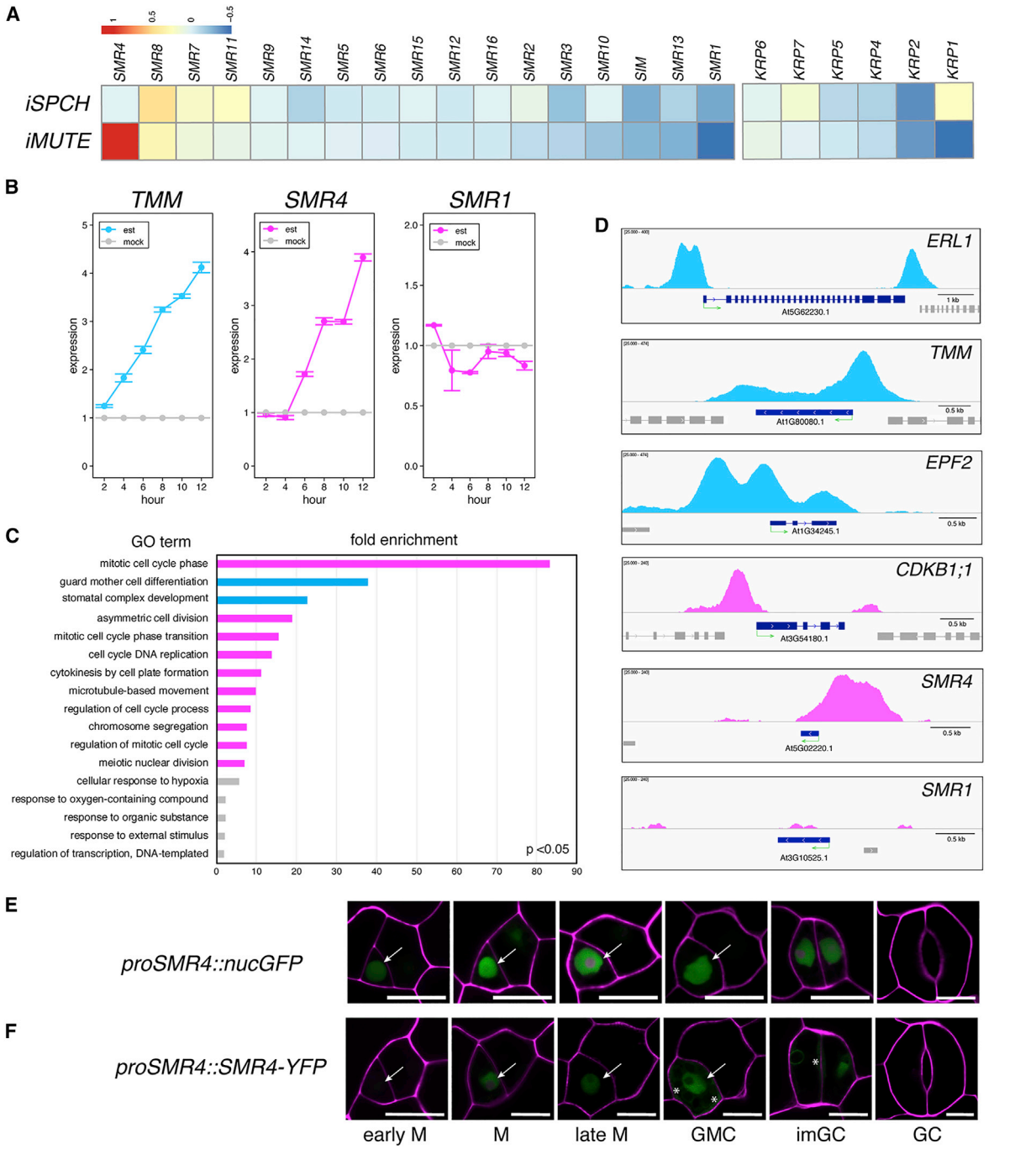

Figure 2. SMR4, one of the plant-specific CKIs expresses in stomatal lineage and is a direct target of MUTE

(A) Heatmap represents the changes in expression of 24 CKIs in Arabidopsis by SPCH or MUTE induction. RNA-seq data adapted from (Lau et al., 2014) (*iSPCH*) and (Han et al., 2018) (*iMUTE*). Heatmap denotes $\log_2$ ratio of changes in expression compared with non-induced control.

(B) Time course expression for 12 h with 2-h interval of *SMR4* and *SMR1* by iMUTE monitored by qRT-PCR. *TMM* was used as a positive control for a MUTE inducible gene. est: 10 μM estradiol treated, mock: non-treated control (DMSO only). Data are presented as mean ± SEM.

(C) GO categories of direct MUTE targets (MUTE bound, iMUTE up) ranked by fold enrichment compared with background genome. $p < 0.05$. Pink bars: "cell cycle," "division," "mitotic" categories; blue bars: "stomatal" categories; gray bars: others.

(D) IGV snapshots of ChIP-seq profile of MUTE binding to the promoters of *SMR4*, *SMR1*, and known MUTE targets (*ERL1*, *TMM*, *EPF2*, and *CDKB1;1*) (Han et al., 2018; Qi et al., 2017). No MUTE binding was detected to *SMR1* loci. A green arrow under the gene annotation indicates gene orientation and transcriptional start sites.

(E and F) Expression patterns of *SMR4* transcriptional and translational reporters. *proSMR4::nucGFP* (E) and *proSMR4::SMR4-YFP* (F) in stomatal lineage precursor cell specific on the epidermis. White arrows: nuclei with GFP or YFP signal. Asterisks: cytoplasmic YFP signal. Scale bar, 10 μm.

See also Figures S2 and S3 and Table S2.

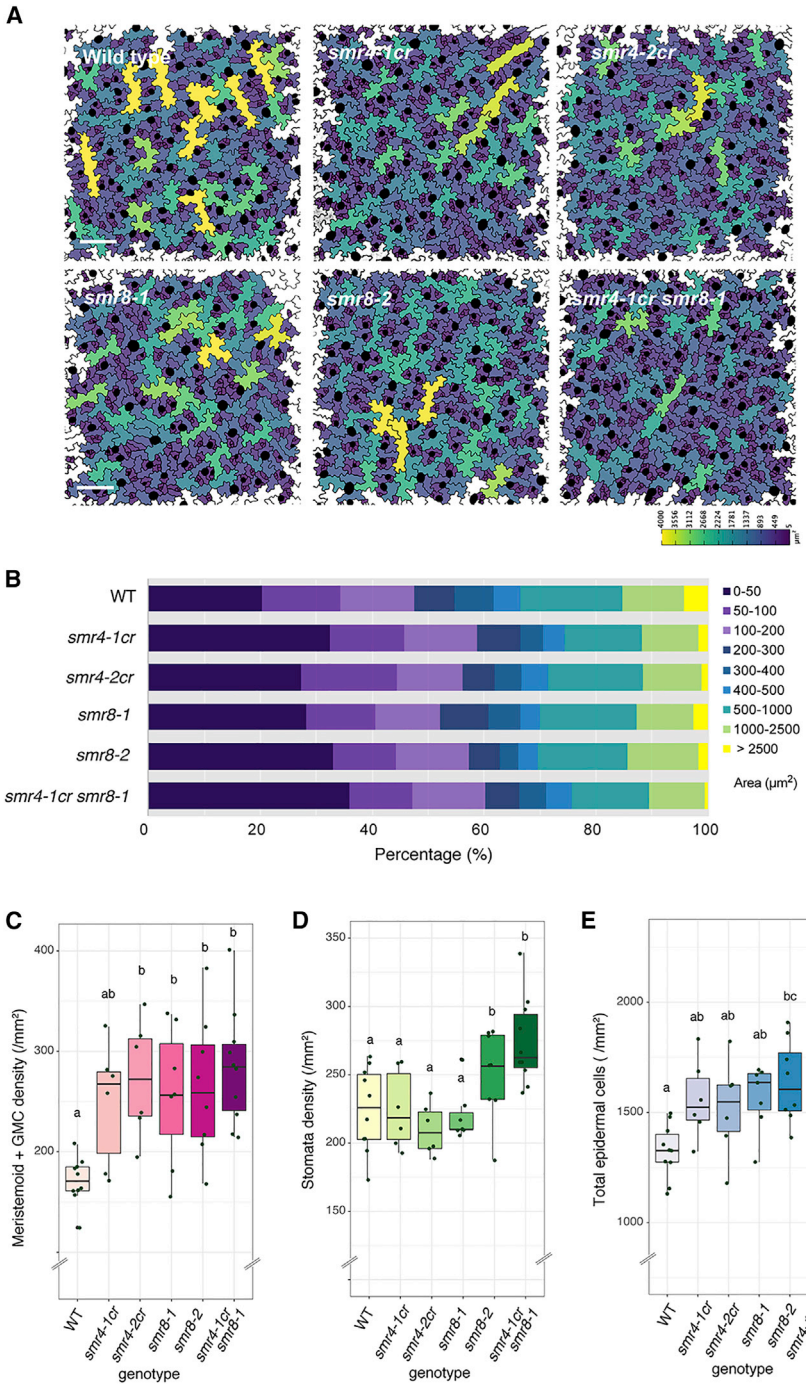

Figure 3. *smr4* CRISPR knockout mutants produce smaller cells, the phenotype is enhanced by *smr8*

(A) Abaxial cotyledon epidermis from 4-day-old seedlings of wild type, *smr4-1cr*, *smr4-2*cr, *smr8-1*, *smr8-2,* and *smr4-1cr smr8-1*double mutant. Epidermal cells size is color coded as a color scale at bottom. GCs are marked in black. Scale bar, 100 μm.

(B) Bar graphs showing the percentage of each category of cell area (rightmost) from the images for the genotype presented in (A). GCs are not included in the category of cell area.

(C–E) Density of stomatal precursor cells (meristemoid+GMC) (C), stomata (D), and total epidermal cell (E) 1.0 mm^{-2} area for the genotypes shown in (A). One-way ANOVA followed by Tukey's post hoc test was performed for comparing all genotypes. Different letter denotes significant difference. Double letter denotes insignificance. $p < 0.05$ or $p < 0.01$. The number of plants from each genotype, WT: n = 10, *smr4-1cr*: n = 6, *smr4-2cr*: n = 6, *smr8-1*: n = 7, *smr8-2*: n = 8, *smr4-1cr smr8-1*: n = 10.

See also Figure S4.

analysis of segmented epidermal cells (see STAR Methods) revealed that *smr4cr* epidermis is increased in small cells (<50 μm^2) and concomitantly decreased in large pavement cells (>4,000 μm^2) (Figures 3A, 3B, and 3E). Stomatal precursor cell (meristemoid and GMC) density is also increased in *smr4cr* alleles (Figure 3C). On the other hand, stomatal density was not significantly changed in *smr4cr* (Figure 3D), suggesting that SMR4 primarily restricts the divisions of early stomatal precursor cells. Introduction of functional *SMR4* transgene (*proSMR4::HA-SMR4*) fully rescued the phenotypes of *smr4-1cr* (Figures S4D–S4G), indicating that increased numbers of stomatal precursor cells in *smr4* mutant are due to the loss of function of *SMR4*.

Because *SMR8* expression was marginally increased by iMUTE (Figure S2), we further characterized the loss-of-function phenotypes of *SMR8*. Two T-DNA insertion lines, *smr8-1* and *smr8-2*, accumulate a reduced-level of *SMR8* transcripts (Figure S4C). Like *smr4*, *smr8* mutants conferred an increase in small epidermal and stomatal precursor cells (Figures 3A–C, and 3E), and the total epidermal cell numbers become most exaggerated in the *smr4 smr8* double mutant (Figure 3E). Therefore, *SMR4* plays a role in repressing ACD in part redundantly with *SMR*8.

SMR4 suppresses cell proliferation in part with *SMR8*

To understand the role of *SMR4* in stomatal development, we next sought to characterize its loss-of-function phenotypes. Because no T-DNA insertion line is available for *SMR4*, presumably owing to its short coding sequence (219 bp), we employed CRISPR-Cas9 system (Tsutsui and Higashiyama, 2017) (see STAR Methods). A guide RNA targeting to *SMR4* yielded either a base-pair deletion (*smr4-1cr*) or insertion (*smr4-2cr*) at 80 bp from the translation start site, which leads to a frameshift and premature stop codon (Figures S4A and S4B). A quantitative

Stomatal-lineage-specific expression of CKIs reveals their unique functions

Our study revealed that *SMR4* is a direct MUTE target and expresses during the transition from proliferating meristemoid state

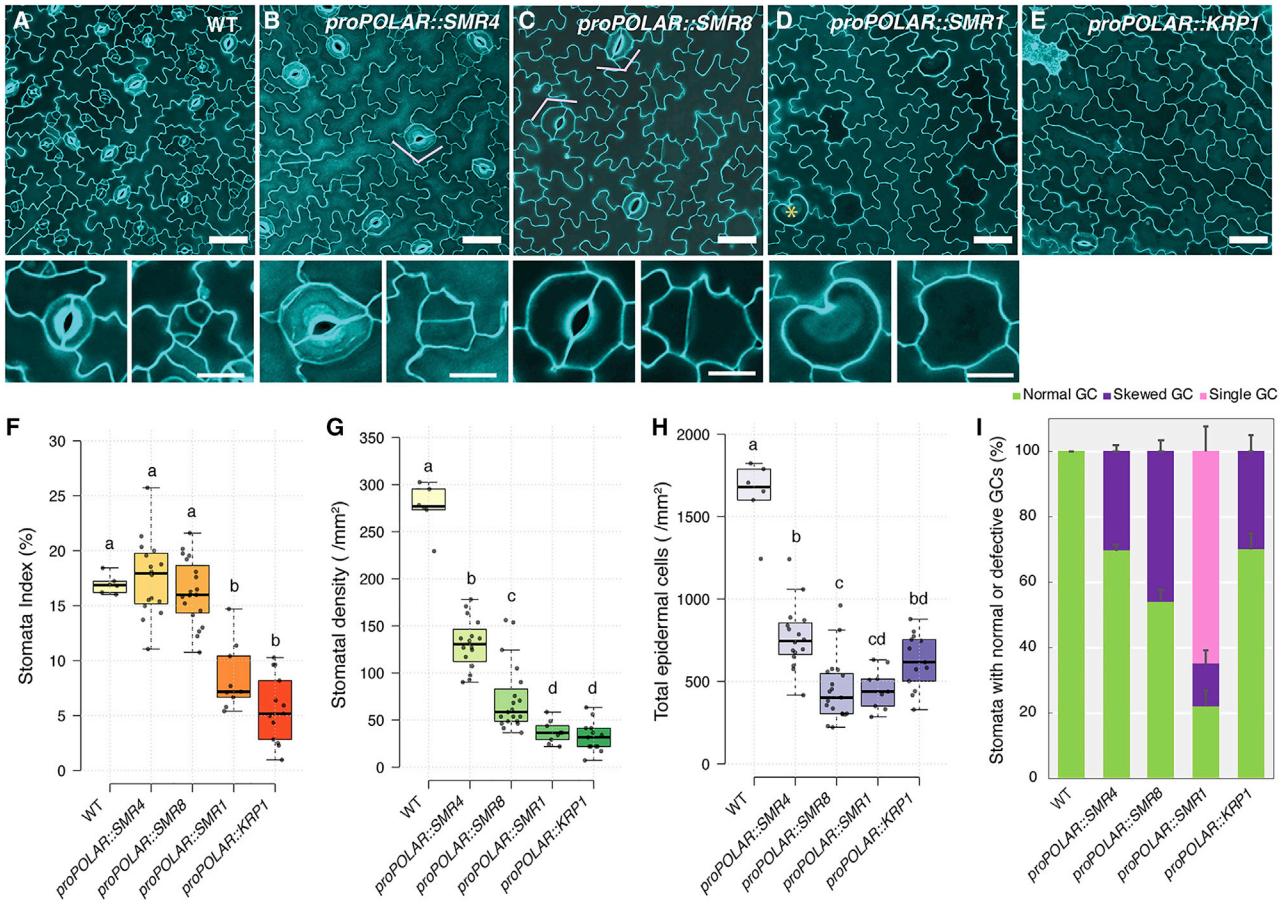

Figure 4. Stomatal lineage overexpression phenotype of a suite of CKIs reveal their unique activities

(A–E) Epidermal phenotype of abaxial cotyledons from 4-day-old wild type (A), *proPOLAR*::*SMR4* (B), *proPOLAR*::*SMR8* (C), *proPOLAR*::*SMR1* (D), and *proPOLAR*::*KRP1* (E). Scale bars, 50 μm. Insets: enlarged mature guard cell and precursor cells from each genotype. Scale bars, 20 μm. Orange asterisks, undivided single-celled stomata. Pink brackets, skewed stomata.

(F–I) Quantification of epidermal cell number of abaxial cotyledon from 4-day-old wild-type and transgenic plants. Stomatal index (F), stomatal density (G), total epidermal cells (H), and fraction of normal (light green), skewed (purple), and single-celled stomata (pink) found on each genotype (I) in 1.0-mm^{-2} area. One-way ANOVA with Tukey's post hoc test was performed to compare all genotypes. The number of plants from each genotype, WT: n = 6, *proPOLAR*::*SMR4*: n = 16, *proPOLAR*::*SMR8*: n = 19, *proPOLAR*::*SMR1*: n = 13, *proPOLAR*::*KRP1*: n = 14.

See also Figure S5.

to differentiating GMC state. SMR proteins are known to promote endoreduplication in trichomes, pavement cells, and sepal giant cells (Hamdoun et al., 2016; Kumar and Larkin, 2017; Roeder et al., 2010; Walker et al., 2000). However, unlike trichomes and pavement cells, stomatal lineage cells do not undergo endoreduplication (Melaragno et al., 1993). We thus hypothesized that SMR4 may function differently from the other canonical SMRs. To address this, *SMR4*, *SMR8*, and *SMR1* along with *KRP1* are ectopically expressed in the stomatal lineage cells (MMC, meristemoids and SLGC) by using *POLAR* promoter (Pillitteri et al., 2011) (Figures 4 and S5). Unlike *SMR1* or *KRP1*, *POLAR*-promoter-driven *SMR4* and *SMR8* did not significantly changed stomatal index ([number of stomata/number of stomata and non-stomatal epidermal cells] ×100) (Figure 4F), reflecting reduction in the number of both stomata and epidermal cells (Figures 4G and 4H). Whereas GMCs of *POLAR*-promoter-driven *SMR4* executed SCD, they occasionally formed stomata composed of skewed guard cells (Figure 4B, pink bracket; Figures 4I and S5). This suggests that SMR4 does not inhibit the final SCD per se. Similar deformed stomata were also observed in *proPOLAR*::*SMR8* (Figure 4C, pink bracket; Figures 4I and S5).

Unlike SMR4, ectopic stomatal lineage expression of SMR1 and KRP1 displayed cell division defects with unique consequences. *proPOLAR*::*SMR1* produced abnormally large undivided GMC-like cells (Figure 4D, asterisks; Figure S5), which constitute over 60% of the all stomata (Figure 4I). This result is consistent with the known role of SMR1 in suppressing the activity of CDKB1;1 thereby promoting endoreduplication (Kumar et al., 2015). Finally, *proPOLAR*::*KRP1* severely inhibited the ACDs, resulting in epidermis vastly consisted of pavement cells with low stomatal index (Figures 4E and 4F), resembling *spch* mutant (MacAlister et al., 2007; Pillitteri et al., 2007). Among those *proPOLAR*::*KRP1* stomata, approximately one-third were deformed (Figure 4I).

CellPress
OPEN ACCESS

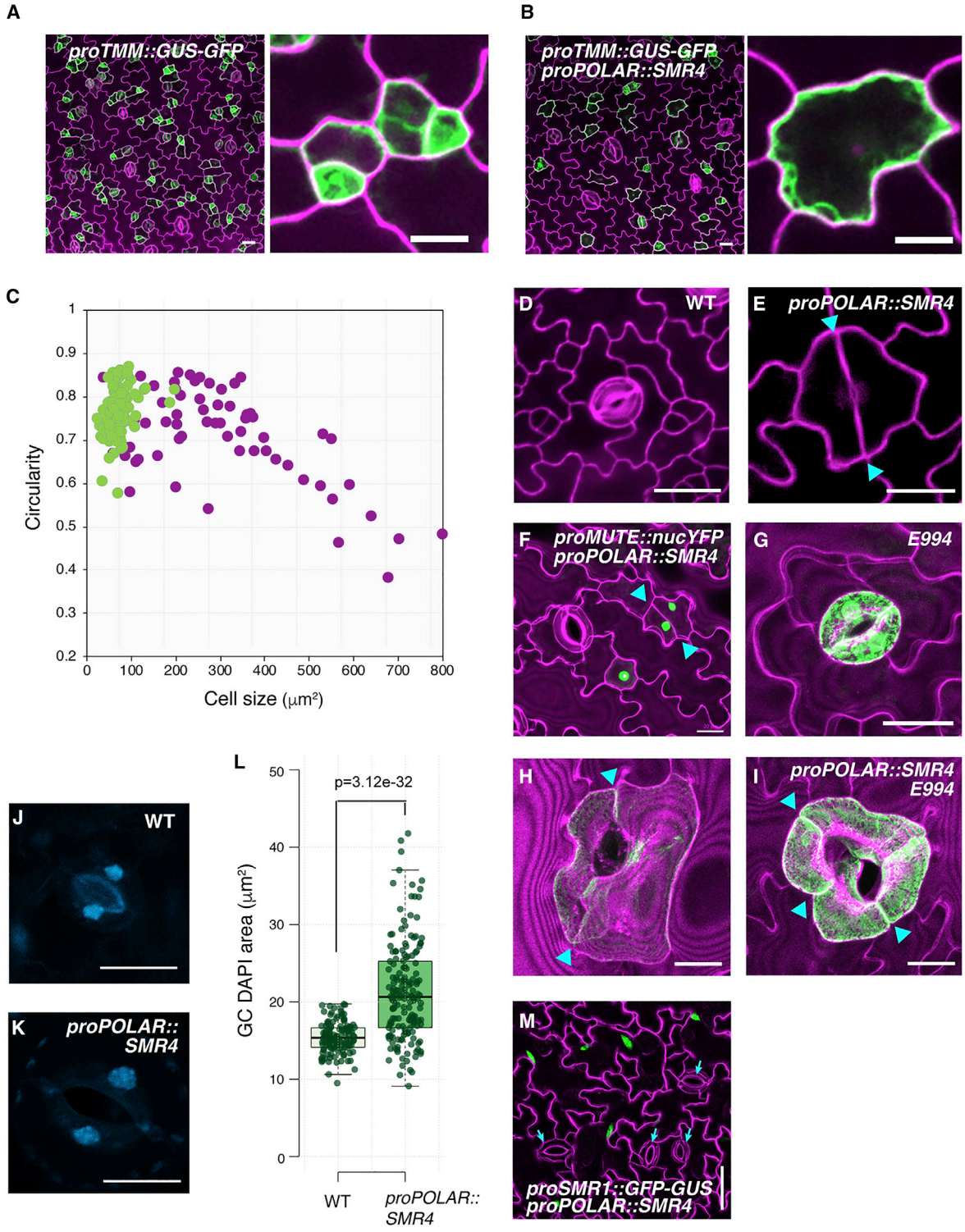

Figure 5. Stomatal lineage overexpression of *SMR4* reduces proliferative activity of meristemoids

(A and B) (A) *proTMM*::*GUS-GFP* abaxial cotyledon from 4-day post-germination stage seedling (4 dpg), (B) *proTMM*::*GUS-GFP* in *proPOLAR*::*SMR4*, 4dpg, Scale bar, 20 μm. Insets: zoomed stomatal lineage cells expressing GFP. Scale bar, 10 μm.

(C) Size distribution versus circularity of the stomatal lineage precursor cells expressing *proTMM*::*GUS-GFP* in wild-type (green dots) and *proPOLAR*::*SMR4* (purple dots) plants.

(D–I) Confocal images of representative stomata: wild-type stoma (D), mixed fate stoma developed *proPOLAR*::*SMR4* (E), *proMUTE*::*nYFP* in *proPOLAR*::*SMR4* (F), mature GC marker *E994* in wild type (G), and *proPOLAR*::*SMR4* (H and I). Cyan arrowheads, division site of GCs. Scale bars, 20 μm.

(legend continued on next page)

The phenotype of *proPOLAR*::*SMR4* (and *SMR8*) is consistent with the diminished proliferative activity of meristemoids. To uncouple formative step from differentiation, we introduced *proPOLAR*::*SMR4* into *mute* mutant, in which a number of amplifying ACDs are increased and meristemoids arrest (Pillitteri et al., 2007) (Figure S5). Indeed, *proPOLAR*::*SMR4* significantly reduced the number of ACDs, resulted in low number of larger meristemoids (Figures S5J–S5N). Since *MUTE* is absolutely required for GMC identity (Pillitteri et al., 2007), these enlarged meristemoids never became stomata. Taken together, we conclude that SMR4, to some extent SMR8, possesses a unique feature different from canonical CKIs to specifically terminate (but not fully inhibit) ACDs of meristemoids but allow final SCD to proceed in GMC. Furthermore, the formation of skewed irregular-shaped stomata, some resembling pavement cells (Figure 4B), implies that excessive SMR4 activity disrupts guard cell morphogenesis.

SMR4 balances between cell proliferation and differentiation

To further understand the identity of abnormally shaped stomata observed in *proPOLAR*::*SMR4*, stomatal lineage markers were introduced. In wild type, stomatal lineage precursor marker *proTMM*::*GUS-GFP* (Nadeau and Sack, 2002) was detected in stomatal lineage cells with the brightest signal in triangular shaped meristemoids (Figure 5A). Surprisingly, both stomatal lineage cells and enlarged pavement cell-like cells in *proPOLAR*::*SMR4* plants expressed *proTMM*::*GUS-GFP* (Figures 5B and S6). Some of these GFP-expressing cells in *proPOLAR*::*SMR4* plants divide symmetrically even without ACD or after a single round of ACD with significantly extended duration (Figures 5B, 5E, and 5F cyan arrows, Figure S6 pink arrows; Video S2). Further quantitative analysis shows that, compared with wild type, these *proTMM*::*GUS-GFP*-positive cells in *proPOLAR*::*SMR4* are greater in size range (50∼800 μm^2) and in addition have low circularity (Figure 5C). This might reflect mixed cell fate, pavement cell shape with stomatal identity. Some of these cells express stomatal fate commitment marker *proMUTE*::*nucYFP* (Figure 5F) and finally differentiate into mature guard cells (Figures 5G–5I) exhibiting large wavy and skewed shape (Figures 5H and 5I) but expressing a mature guard cell marker, E994. Thus, the large skewed GCs in *proPOLAR*::*SMR4* originate from the enlarged stomatal lineage precursors caused by delayed and fewer ACD cycles (Figure S6; Video S2).

To address whether these enlarged GCs undergo endoreduplication process when *SMR4* is ectopically expressed, the DNA content was measured using DAPI fluorescence (Figures 5J–5L). Half of GC populations exhibited the fluorescence similar to the wild type (the median value is 15 μm^2 in wild type and 20 μm^2 in *proPOLAR*::*SMR4* plants), whereas some showed fluorescence values nearly doubled in *proPOLAR*::*SMR4* plants (Figures 5J–L). Likewise, the GC nuclei size measurements using H2B-GFP (Maruyama et al., 2013) are consistent with the DAPI measurements (Figures S7A–S7D). The difference in nuclei size was more pronounced in pavement cells. Furthermore, none of the GCs expresses the endoreduplication marker *proSMR1*::*nlsGFP-GUS* (Bhosale et al., 2018) regardless of the GC size in *proPOLAR*::*SMR4* plants, whereas pavement cells, where endoreduplication normally occurs, express GFP signal (Figure 5M). Combined, these results suggest that stomatal lineage overexpression of SMR4 may confer doubled DNA content, probably due to cell-cycle arrest in G2 after the S phase. Unlike SMR1, however, SMR4 does not trigger the endoreduplication cycle in the stomatal lineage. This feature distinguishes SMR4 from the known SIM/SMR-family of CKIs. The unique, non-canonical activity of SMR4 is also supported by systematic stomatal lineage overexpression of selected CKIs, where only SMR1 generated huge undivided GMC cells (Figures 4D and S5). Indeed, quantitative analysis showed that the nuclear size of *proPOLAR*::*SMR1* GCs is ∼10 times larger than that of the control wild-type plants (Figures S7E–S7H), consistent with the known role of SMR1 in triggering endoreduplication (Hamdoun et al., 2016; Kumar et al., 2015; Schwarz and Roeder, 2016).

SMR4 decelerates cell-cycle progression by G1 phase extension

We elucidated that stomatal lineage ACDs are faster than the final SCD (Figures 1B and 1C). What is the ramification of stomatal lineage overexpression or loss-of-function mutation of *SMR4* on cell-cycle duration of ACDs and SCD? To address this question, we introduced PlaCCI to *proPOLAR*::*SMR4* and *smr4-1cr* mutant plants and performed time-lapse imaging (Figure 6; Videos S3 and S4). The stomatal precursor cells (meristemoids) in *proPOLAR*::*SMR4* seedlings showed extended ACD cycle duration from 12.00 to 18.47 h (Figures 6A, 6B, and 6G; Table S1). This made the ACD cycle duration statistically non-significant from that of the SCD (Figure 6A). Further analysis of cell-cycle phase emphasized the striking extension of G1 phase, as determined by the time window from the onset of CDT1a-CFP expression to HTR13-mCherry expression (Desvoyes et al., 2020) (Figures 6B and 6C), from average of 3.73 to 7.97 h (Figure 6I; Video S3; Table S1). In contrast, the cell-cycle duration of the SCD was not significantly affected by *proPOLAR*::*SMR4* (19.57 h, Figures 6A and 6C; Video S3; Table S1).

During the ACD in *smr4-1cr* mutant, the G1 phase became shortened by 1 h compared with wild type (Figures 6E and 6I; Table S1; Video S4, WT: 3.73 h versus *smr4-1cr*: 2.73 h) while the S/G2 and M phases remained unchanged (Table S1), indicating that, in the absence of SMR4, the ACD cell cycle becomes accelerated. Again, the cell-cycle duration or the G1 phase duration of SCD was not significantly changed by the *smr4-1cr* mutation (Figures 6D, 6F, 6H, and 6J; Video S4; Table S1). Taken together, the results highlight that SMR4 is both necessary and sufficient to slow down cell-cycle progression by G1 phase extension, to prevent the further occurrence of ACDs once stomatal differentiation has been committed.

(J and K) DAPI-stained nuclei in mature GCs from wild-type (J) and *proPOLAR*::*SMR4* plants (K).
(L) Quantitative analysis of DAPI-stained nuclear area in wild-type and *proPOLAR*::*SMR4* GCs. Two-tailed Student's t test was performed. $p = 3.12e^{-32}$.
(M) Endoreduplication marker *proSMR1*::*GFP-GUS* expression in *proPOLAR*::*SMR4* plants. Cyan arrows indicate enlarged GCs with no GFP expression. Scale bar, 50 μm.
See also Figures S6 and S7.

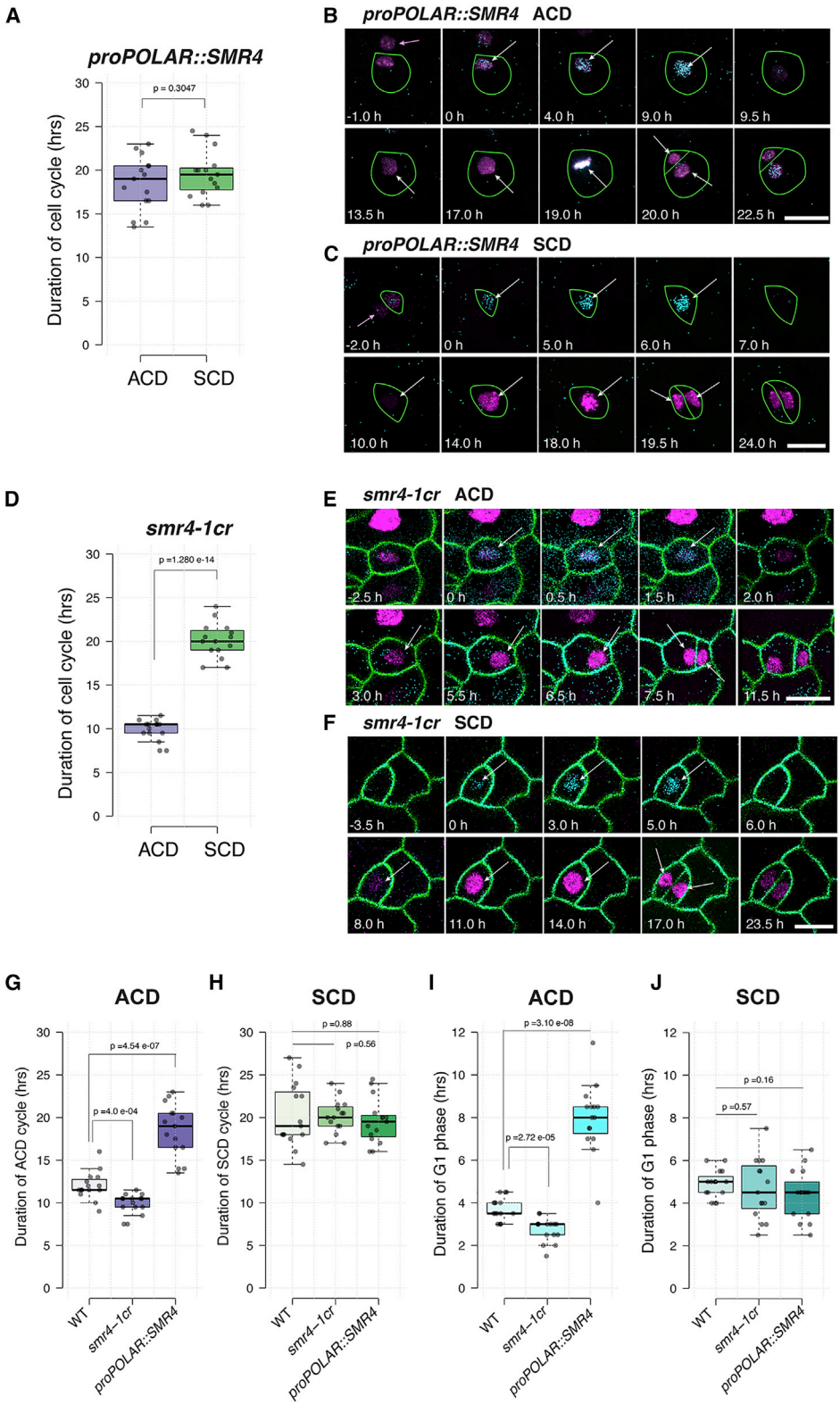

Figure 6. SMR4 slows down the cell-cycle progression of ACD through G1 extension

(A and D) Cell-cycle duration of ACD and SCD measured by PlaCCI in *proPOLAR*::*SMR4* (A) and *smr4-1cr* (D). n = 15 for each cell division mode.

(B, C, E, and F) Representative time-lapse confocal images of ACD and SCD in stomatal lineage cells from 1 to 3-day-old cotyledon of *proPOLAR*::*SMR4* (B and C) and *smr4-1cr* (E and F) expressing PlaCCI. Cell outlines (green) for *proPOLAR*::*SMR4* (B and C) were hand-drawn based on digital overexposure of confocal

(legend continued on next page)

Physical and functional interactions of SMR4 with D-type cyclins underscore the switch from ACD to SCD

SIM is known to interact with CYCA2;3 to promote endoreduplication (Wang et al., 2020). Unlike SIM, stomatal lineage overexpression of *SMR4* can extend G1 cycles of ACD but allow execution of the final SCD (Figures 4, 5, and 6). We thus predict that SMR4 regulates the G1-S transition via associating with CyclinDs. To understand the mode of action of SMR4, we first surveyed publicly available protein-protein interactome data (Szklarczyk et al., 2019), including a large-scale Arabidopsis *in vivo* mass-spectrometry-based interactome profiling of cell-cycle components through tandem-affinity purification-based technology (Van Leene et al., 2010). The known SMR4 interactors include major components of cell-cycle progression, CSK1, CKS2, CDKA;1 (CDC2), CYCD2;1, CYCD3;1 and CYCD7;1 (Van Leene et al., 2010) (Figure 7A). Among them, CYCD3;1 activity rises when cell re-enter the cell cycle (Riou-Khamlichi et al., 1999) and is highly induced by SPCH (Adrian et al., 2015), whereas CYCD7;1 is involved in the SCD of GMC (Weimer et al., 2018). Our yeast two-hybrid (Y2H) analysis shows that consistent with the interactome data (Figure 7A), SMR4 associates with CYCD3;1 and CYCD7;1 (Figure 7B). In contrast, no interaction was observed for SMR4 and CYCD5;1, a direct MUTE target initiating the single SCD (Han et al., 2018) (Figure 7B). We also did not observe the direct interaction of SMR4 with CDKA;1 or CDKB1;1 (Figure 7B).

Next, to address the biological significance of SMR4 interactions with CYCD3;1 and CYCD7;1 but not with CYC5;1, we examined the effects conferred by stomatal lineage overexpression of three CyclinDs in the presence or absence of functional *SMR4*. As shown in Figures 7C and 7D, in the absence of *SMR4*, *POLAR*-promoter-driven expression of *CYCD3;1* and *CYCD7;1* exaggerated the ACDs, resulting in significant increase in the density of stomatal precursor cells. Importantly, *proPOLAR::CYCD3;1* did not influence the stomatal precursor cell density in wild type (which carries functional *SMR4*), whereas the ratio of the precursor cell density between wild type and *smr4-1cr* became greater in the presence of *proPOLAR::CYCD3;1* (1.24 to 1.65). These results suggest that increase of stomatal precursors by CYCD3;1 requires the absence of SMR4 (Figure 7D). By contrast, *proPOLAR::CYCD5;1* increased the stomatal precursor cells regardless of the presence or absence of *SMR4*, indicating that CYCD5;1 activity is SMR4-independent (Figures 7C and 7D). On the basis of these findings, we conclude that SMR4 can suppress the stomatal lineage divisions by direct association with CYCD3;1 and possibly with CYCD7;1, but not with CYCD5;1, and this differential interaction with CyclinDs underscores the transition from proliferative ACDs to final SCD (Figure 7E).

DISCUSSION

In this study, we discovered that proliferative ACDs has faster cell-cycle duration than the single terminal SCD within the stomatal cell lineages. A subsequent genome-wide profiling of MUTE targets followed by phenotypic and functional characterizations identified SMR4 as a non-canonical CKI that sets a cell-cycle brake to facilitate transition from ACD to SCD. *SMR4* is a direct MUTE target specifically induced by MUTE but not by SPCH (Figure 2), thus highlighting the orchestration of cell-state switch from proliferation (meristemoids) to differentiation (stomata) at the control of cell-cycle duration. This view is further supported by the findings that prolonged G1 phase specifically during the proliferative ACDs by stomatal lineage overexpression of *SMR4* causes misspecification of guard cells (Figures 4 and 5).

In contrast of SIM and SMR1, known regulators of endoreduplication (Roeder et al., 2010; Wang et al., 2020), we found that SMR4 delays the G1/S transition during stomatal ACDs (Figure 6). It has been shown that SIM associates with CYCA2;3 but not with CYCD3;1 (Wang et al., 2020). Assuming that SMR1 functions similarly to SIM, the enlarged single-celled stomata conferred by the stomatal lineage overexpression of SMR1 (Figure 4) can be attributed to the direct inhibition of CYCA2;3-CDKB;1 complex by SMR1. Indeed, higher-order mutations in *CYCA2s* (*cycA2;1*, *2;2*, *2,3* triple mutant) as well as the dominant-negative inhibition of *CDKB1;1* exhibit the identical, single-celled stomata phenotypes (Boudolf et al., 2004; Vanneste et al., 2011). By contrast, we found that SMR4 functionally associates with CyclinDs (Figure 7). Thus, distinct functions among SIM/SMRs lie in their unique interaction potential with different cyclin-CDK complexes. During mammalian cell cycle, a series of CKIs exhibit inhibitory roles during G1/S transition via associating with CyclinD1/2/3-CDK4/6 and then with CyclinE/CDK2 complexes (Sherr and Roberts, 2004). Among them, $p27^{KIP1}$ can bind with multiple cyclin-CDK complexes and exert different regulatory effects on each complex (Sherr and Roberts, 2004). Plants lack CyclinE, but the previous large-scale expression analysis of cell-cycle genes suggests that the plant CYCDs adopt both metazoan CyclinD and CyclinE functions (Menges et al., 2005). That SMR4 binds with different CyclinDs to negatively regulate G1/S phase therefore echoes its functional parallel to metazoan CKI, $p27^{KIP1}$.

How could SMR4 decelerate cell cycle in proliferative ACDs but not in terminal SCD? Our results suggest that the specificity lies on preferential association of SMR4 with different CyclinDs, each with a unique expression pattern within the stomatal cell lineages. For example, *CYCD3;1* and *CYCD3;2* are induced by *SPCH* and promote ACDs (Adrian et al., 2015; Dewitte et al., 2007; Han et al., 2018; Lau et al., 2014). By contrast, *CYCD5;1* is directly induced by MUTE to drive the terminal SCD (Han et al., 2018). *CYCD7;1* is likely involved in the terminal SCD, however, its expression starts later and persists longer than *CYCD5;1* (Han et al., 2018; Weimer et al., 2018). Based on the physical and functional associations of SMR4 with CYCD3;1 and CYCD7;1 but not with CYCD5;1, we propose the following model of regulatory circuit driving the asymmetric-to-symmetric

images. LTi6B (green) are introduced into *smr4-1cr* (E and F). For the color code and time setting, see Figure 1 legends. White arrows indicate the nuclei with fluorescent signal. Pink arrows indicate the nucleus of a sister cell from the prior round of ACD. Scale bar, 10 μm.
(G and H) Cell-cycle duration of ACD (G) and SCD (H) among WT, *smr4-1cr* and *proPOLAR::SMR4*.
(I and J) G1 phase duration of ACD (I) and SCD (J) among WT, *smr4-1cr*, and *proPOLAR::SMR4*.
(A, D, G, H, I, and J) Two-tailed Student's t test was performed. p values were indicated on top of each boxplot.
See also Table S1, and Videos S3 and S4.

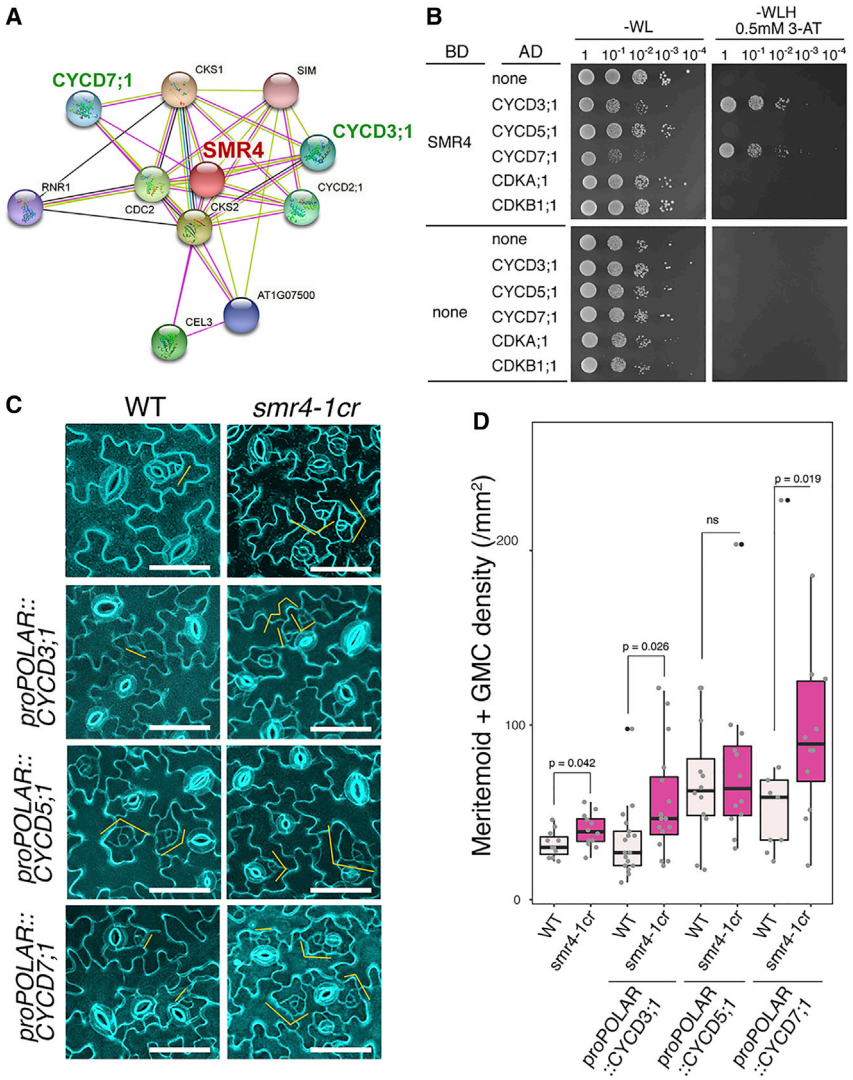

Figure 7. SMR4 decelerates the cell cycle via direct interactions with a selected set of D-type cyclins

(A) SMR4 interacting proteins from *in vivo* interactome (Van Leene et al., 2010) visualized by cytoscape.

(B) Yeast two-hybrid assays. Bait, the DNA-binding domain (BD) alone or fused to SMR4. Prey, the activation domain alone (AD) or fused to CYCD3;1, CYCD5;1, CYCD7;1, CDKA;1, and CDKB1;1. Transformed yeast were spotted in 10-fold serial dilutions on appropriate selection media.

(C) Transgenic plants harboring CYCD3;1, CYCD5;1, and CYCD7;1 driven by the *POLAR* promoter in wild type (WT) and *smr4-1cr* in comparison with wild type and *smr4-1cr*. Orange brackets: stomatal lineage precursors. Scale bars, 50 μm.

(D) Quantification of stomatal precursor cells in 1.0 mm^{-2} area from 7-day-old seedlings. Mann-Whitney test was performed. p values were marked on top of the boxplot. Independent T1 transgenic plants were analyzed. The number of plants used: WT: n = 11, *smr4-1cr*: n = 12, *proPOLAR*::*CYCD3*;1: n = 17, *proPOLAR*::*CYCD3*;1 *smr4-1cr*: n = 16, *proPOLAR*::*CYCD5*;1: n = 12, *proPOLAR*::*CYCD5*;1 *smr4-1cr*: n = 12. *proPOLAR*::*CYCD7*;1: n = 9, *proPOLAR*::*CYCD7*;1 *smr4-1cr*: n = 12.

(E) Schematic model. SPCH·SCRM/2 initiate and sustain ACD and MUTE·SCRM/2 trigger SCD (gray arrows) by transcriptionally activating *CYCD3;1* and *CYCD5;1* (shaded blue arrows), respectively. MUTE directly up-regulates *SMR4* transcription (Blue arrow). SMR4 (and SMR8 in part) suppress the activity of CYCD3;1 and possibly CYCD7;1 complexed with CDKs (red line), but not CYCD5;1, to terminate the ACD mode and ensure faithful progression of SCD. Question marks and dotted line indicate the possible roles of SMR8 in termination of ACD and SMR4 with CYCD7;1 in symmetric cell division, respectively.

division switch (Figure 7E): First, SPCH initiates and sustains the fast and reiterative ACDs of a meristemoid. During the meristemoid-to-GMC transition, MUTE directly induces SMR4, which directly associates with CYCD3;1 (and likely with CYCD3;2) and inhibit CYCD3;1-CKDA;1 complex to terminate amplifying ACDs. At the same time, MUTE directly induces CYCD5;1. Because CYCD5;1 is not directly inhibited by SMR4, the final SCD can start even in the presence of SMR4. SMR4 may fine-tune the SCD by being able to inhibit the later-expressed CYCD7;1, which is likely complexed with CDKA;1. The endogenous expression of SMR4 disappears immediately after the execution of SCD (Figure 2F); hence, the robust differentiation of stomata ensured. SMR8 has partially redundant role with SMR4 and is weakly induced by both SPCH and MUTE (Figures 2 and S2) as such, SMR8 is likely participating in fine-tuning of this transition. Unlike CycD3s and CycD7;1, CycD5;1 lacks part of the core domain (Strzalka et al., 2015), which may explain the differential SMR4 binding.

In addition to CKIs, Rb protein negatively regulates G1/S transition (Bertoli et al., 2013). The plant RETINOBLASTOMA RELATED (RBR) protein functions as key cell-cycle regulators during stomatal development, and its reduced expression confers excessive proliferative ACDs within the stomatal cell lineages, in part due to dysregulated *SPCH* expression (Borghi et al., 2010; Weimer et al., 2012). Whereas both CYCD3;1 and CYCD7;1 possess LxCxE RBR-binding motif, CYCD5;1 bears a variant motif, which may compromise the RBR association (Vandepoele et al., 2002). Thus, CYCD5;1's unique activity to execute the single SCD might involve the lack of negative regulation by RBR. Interestingly, RBR regulates the expression and activities of stomatal bHLH proteins, SPCH, and FAMA, respectively (Matos et al., 2014; Weimer et al., 2012), but not MUTE. Thus, the commitment to differentiation by MUTE-orchestrated network may be inherently resilient to inhibition at G1/S transition.

Our study showed that extended G1 phase by stomatal lineage overexpression of SMR4 conferred irregular-shaped meristemoids and eventual differentiation of stomata with skewed guard cells. Some guard cells exhibit a jigsaw-puzzled shape, which is indicative of pavement cell-like characteristics (Figures 4 and 5). Thus, without timely execution of an ACD, the stomatal precursor cell can adopt hybrid identity of a guard cell and pavement cell. An intrinsic polarity protein BASL ensures that only one of the two daughter cells, the meristemoid, maintains high SPCH levels, thereby able to reiterate proliferative ACDs (Dong et al., 2009). The remaining daughter cell readily loses SPCH protein and differentiate into a pavement cell. This process involves a dynamic subcellular re-localization of BASL protein between the nucleus and polarly localized cell cortex, the latter activates MAP kinase cascade that inhibits SPCH protein accumulation via phosphorylation (Zhang et al., 2015, 2016). It is not known whether the cell-cycle phase influences BASL behaviors, but our work implies that it could be the case.

The SMR4-mediated cell-cycle deceleration during the meristemoid-to-GMC transition mirrors the fundamental importance of G1-phase extension for cell fate decision and differentiation during development (Dalton, 2015; Liu et al., 2019). During mammalian adipogenesis, commitment of proliferating precursors to terminal differentiation is governed by the molecular competition of mitogens and differentiation stimuli at the G1-phase, in which timing determines the final numbers of adipocytes (Zhao et al., 2020). During plant stomatal differentiation, we found that the timing of G1-phase is not only critical for the commitment to differentiation but also maintaining the shape and size of stomatal lineage cells. In any event, the fine-tuning of the G1 phase duration may be the universal mechanism for proper cell-type differentiation in multicellular organisms. The direct role of MUTE to execute both termination of proliferative asymmetric divisions and orchestration of the single terminal symmetric division occurs through interwoven regulation of core cell-cycle drivers and a braker. Understanding how cell-cycle machineries in turn regulate the precise expression of MUTE, which likely involves epigenetic state changes, will provide a full picture of cell-cycle control of cell fate specification in plants.

Limitations of the study

We use CDT1a-CFP loading as a proxy for the G1 phase duration. We noticed that in stomatal lineage cells, CDF1a-CFP does not accumulate for the entire G1 phase. Nevertheless, it is clear that ACD is faster than SCD, based on both the quantitative analysis of the actual cell division time and the observed shorter duration of CDT1a-CFP signals in ACDs. In addition, the time-lapse imaging was performed using cotyledons grown under the microscope, and thus, it may not represent the exact cell-cycle time of stomatal precursors in vegetative leaves from field-grown plants.

STAR★METHODS

Detailed methods are provided in the online version of this paper and include the following:

- KEY RESOURCES TABLE
- RESOURCE AVAILABILITY
  - Lead contact
  - Materials availability
  - Data and code availability
- EXPERIMENTAL MODEL AND SUBJECT DETAILS
- METHOD DETAILS
  - Plasmid construction and generation of CRISPR-based mutant alleles
  - Plant growth condition and estradiol treatment
  - Confocal microscopy
  - Quantitative analysis of epidermal phenotype
  - cDNA preparation and qRT-PCR
  - Chromatin immunoprecipitation sequencing (ChIP-seq)
  - Measurement of DNA content and nuclei size
  - Yeast two hybrid assay
- QUANTIFICATION AND STATISTICAL ANALYSIS

SUPPLEMENTAL INFORMATION

Supplemental information can be found online at https://doi.org/10.1016/j.devcel.2022.01.014.

ACKNOWLEDGMENTS

We thank Lieven De Veylder for *proSMR1*::*nls-GFP-GUS*, Daisuke Kurihara for *proRPS5A*::*H2B-GFP*, ABRC for GFP-Lti6B and SMR8 T-DNA lines, and James Green, Machiko Arakawa and Ayami Nakagawa for assistance in plant care. This work is supported by MEXT KAKENHI Grant-in-Aid for Scientific Research on Innovative Areas (17H06476), WPI-ITbM, and the start-up funds from the UT Austin to K.U.T.; grant RTI2018-094793-B-I00 from Spanish Ministry of Science and Innovation and grant 2018-AdG_833617 from European Research Council to C.G. K.U.T. acknowledges the support from Howard Hughes Medical Institute and Johnson & Johnson Centennial Chair in Plant Cell Biology at the UT Austin. S.-K.H. was supported by the Young Leader Cultivation Program from Nagoya University. A.H. is supported by the Walter Benjamin Program, Deutsche Forschungsgemeinschaft (447617898).

AUTHOR CONTRIBUTIONS

Conceptualization, S.-K.H. and K.U.T.; experimental design, S.-K.H., E.-D.K., and K.U.T.; performance of experiments, S.-K.H., A.H., J.Y., R.I., and T.S.; bioinformatics analysis, S.-K.H., S.K., E.-D.K., and K.U.T.; visualization, S.-K.H., A.H., J.Y., and K.U.T.; essential materials and tools, B.D. and C.G.; Writing – original draft, S.-K.H. and K.U.T.; Writing – review & editing, S.-K.H., A.H., J.Y., B.D., C.G., E.-D.K., and K.U.T.; project administration, K.U.T.; funding acquisition, C.G. and K.U.T.

DECLARATION OF INTERESTS

The authors declare no competing interests.

INCLUSION AND DIVERSITY

One or more of the authors of this paper self-identifies as a member of the LGBTQ+ community.

Received: April 27, 2021
Revised: November 19, 2021
Accepted: January 19, 2022
Published: February 10, 2022

REFERENCES

Adrian, J., Chang, J., Ballenger, C.E., Bargmann, B.O., Alassimone, J., Davies, K.A., Lau, O.S., Matos, J.L., Hachez, C., Lanctot, A., et al. (2015). Transcriptome dynamics of the stomatal lineage: birth, amplification, and termination of a self-renewing population. Dev. Cell *33*, 107–118.

Babicki, S., Arndt, D., Marcu, A., Liang, Y., Grant, J.R., Maciejewski, A., and Wishart, D.S. (2016). Heatmapper: web-enabled heat mapping for all. Nucleic Acids Res. *44*, W147–W153.

Bertoli, C., Skotheim, J.M., and de Bruin, R.A. (2013). Control of cell cycle transcription during G1 and S phases. Nat. Rev. Mol. Cell Biol. *14*, 518–528.

Bhosale, R., Boudolf, V., Cuevas, F., Lu, R., Eekhout, T., Hu, Z., Van Isterdael, G., Lambert, G.M., Xu, F., Nowack, M.K., et al. (2018). A spatiotemporal DNA endoploidy map of the Arabidopsis Root reveals roles for the endocycle in root development and stress adaptation. Plant Cell *30*, 2330–2351.

Borghi, L., Gutzat, R., Fütterer, J., Laizet, Y., Hennig, L., and Gruissem, W. (2010). Arabidopsis RETINOBLASTOMA-RELATED is required for stem cell maintenance, cell differentiation, and lateral organ production. Plant Cell *22*, 1792–1811.

Boudolf, V., Barrôco, R., de Almeida Engler, J., Verkest, A., Beeckman, T., Naudts, M., Inzé, D., and De Veylder, L. (2004). B1-type cyclin-dependent kinases are essential for the formation of stomatal complexes in Arabidopsis thaliana. Plant Cell *16*, 945–955.

Budirahardja, Y., and Gönczy, P. (2009). Coupling the cell cycle to development. Development *136*, 2861–2872.

Coronado, D., Godet, M., Bourillot, P.-Y., Tapponnier, Y., Bernat, A., Petit, M., Afanassieff, M., Markossian, S., Malashicheva, A., Iacone, R., et al. (2013). A short G1 phase is an intrinsic determinant of naive embryonic stem cell pluripotency. Stem Cell Res. *10*, 118–131.

Dalton, S. (2015). Linking the cell cycle to cell fate decisions. Trends Cell Biol. *25*, 592–600.

Desvoyes, B., Arana-Echarri, A., Barea, M.D., and Gutierrez, C. (2020). A comprehensive fluorescent sensor for spatiotemporal cell cycle analysis in Arabidopsis. Nat. Plants *6*, 1330–1334.

Desvoyes, B., and Gutierrez, C. (2020). Roles of plant retinoblastoma protein: cell cycle and beyond. EMBO J *39*, e105802.

Dewitte, W., Scofield, S., Alcasabas, A.A., Maughan, S.C., Menges, M., Braun, N., Collins, C., Nieuwland, J., Prinsen, E., Sundaresan, V., and Murray, J.A.H. (2007). Arabidopsis CYCD3 D-type cyclins link cell proliferation and endocycles and are rate-limiting for cytokinin responses. Proc. Natl. Acad. Sci. USA *104*, 14537–14542.

Dong, J., MacAlister, C.A., and Bergmann, D.C. (2009). BASL controls asymmetric cell division in Arabidopsis. Cell *137*, 1320–1330.

Elledge, S.J. (1996). Cell cycle checkpoints: preventing an identity crisis. Science *274*, 1664–1672.

Feng, J., Liu, T., Qin, B., Zhang, Y., and Liu, X.S. (2012). Identifying ChIP-seq enrichment using MACS. Nat. Protoc. *7*, 1728–1740.

Hachez, C., Ohashi-Ito, K., Dong, J., and Bergmann, D.C. (2011). Differentiation of Arabidopsis guard cells: analysis of the networks incorporating the basic helix-loop-helix transcription factor, FAMA. Plant Physiol. *155*, 1458–1472.

Hamdoun, S., Zhang, C., Gill, M., Kumar, N., Churchman, M., Larkin, J.C., Kwon, A., and Lu, H. (2016). Differential roles of two homologous cyclin-dependent kinase inhibitor genes in regulating cell cycle and innate immunity in Arabidopsis. Plant Physiol. *170*, 515–527.

Han, S.-K., Qi, X., Sugihara, K., Dang, J.H., Endo, T.A., Miller, K.L., Kim, E.-D., Miura, T., and Torii, K.U. (2018). MUTE directly orchestrates cell-state switch and the single symmetric division to create stomata. Dev. Cell *45*, 303–315.e5.

Han, S.-K., and Torii, K.U. (2016). Lineage-specific stem cells, signals and asymmetries during stomatal development. Development *143*, 1259–1270.

Harashima, H., Dissmeyer, N., and Schnittger, A. (2013). Cell cycle control across the eukaryotic kingdom. Trends Cell Biol *23*, 345–356.

Houbaert, A., Zhang, C., Tiwari, M., Wang, K., de Marcos Serrano, A., Savatin, D.V., Urs, M.J., Zhiponova, M.K., Gudesblat, G.E., Vanhoutte, I., et al. (2018). POLAR-guided signalling complex assembly and localization drive asymmetric cell division. Nature *563*, 574–578.

Inzé, D., and De Veylder, L. (2006). Cell cycle regulation in plant development. Annu. Rev. Genet. *40*, 77–105.

James, P., Halladay, J., and Craig, E.A. (1996). Genomic libraries and a host strain designed for highly efficient two-hybrid selection in yeast. Genetics *144*, 1425–1436.

Koncz, C., Németh, K., Rédei, G.P., and Schell, J. (1992). T-DNA insertional mutagenesis in Arabidopsis. Plant Mol. Biol. *20*, 963–976.

Kumar, N., Harashima, H., Kalve, S., Bramsiepe, J., Wang, K., Sizani, B.L., Bertrand, L.L., Johnson, M.C., Faulk, C., Dale, R., et al. (2015). Functional conservation in the SIAMESE-RELATED family of cyclin-dependent kinase inhibitors in land plants. Plant Cell *27*, 3065–3080.

Kumar, N., and Larkin, J.C. (2017). Why do plants need so many cyclin-dependent kinase inhibitors? Plant Signal. Behav. *12*, e1282021.

Kurup, S., Runions, J., Köhler, U., Laplaze, L., Hodge, S., and Haseloff, J. (2005). Marking cell lineages in living tissues. Plant J *42*, 444–453.

Langmead, B., and Salzberg, S.L. (2012). Fast gapped-read alignment with Bowtie 2. Nat. Methods *9*, 357–359.

Lau, O.S., and Bergmann, D.C. (2012). Stomatal development: a plant's perspective on cell polarity, cell fate transitions and intercellular communication. Development *139*, 3683–3692.

Lau, O.S., Davies, K.A., Chang, J., Adrian, J., Rowe, M.H., Ballenger, C.E., and Bergmann, D.C. (2014). Direct roles of SPEECHLESS in the specification of stomatal self-renewing cells. Science *345*, 1605–1609.

Li, H., Handsaker, B., Wysoker, A., Fennell, T., Ruan, J., Homer, N., Marth, G., Abecasis, G., and Durbin, R.; 1000 Genome Project Data Processing Subgroup (2009). The Sequence Alignment/Map format and SAMtools. Bioinformatics *25*, 2078–2079.

Liu, L., Michowski, W., Kolodziejczyk, A., and Sicinski, P. (2019). The cell cycle in stem cell proliferation, pluripotency and differentiation. Nat. Cell Biol. *21*, 1060–1067.

MacAlister, C.A., Ohashi-Ito, K., and Bergmann, D.C. (2007). Transcription factor control of asymmetric cell divisions that establish the stomatal lineage. Nature *445*, 537–540.

Maruyama, D., Hamamura, Y., Takeuchi, H., Susaki, D., Nishimaki, M., Kurihara, D., Kasahara, R.D., and Higashiyama, T. (2013). Independent control by each female gamete prevents the attraction of multiple pollen tubes. Dev. Cell *25*, 317–323.

Matos, J.L., Lau, O.S., Hachez, C., Cruz-Ramírez, A., Scheres, B., and Bergmann, D.C. (2014). Irreversible fate commitment in the Arabidopsis stomatal lineage requires a FAMA and RETINOBLASTOMA-RELATED module. Elife *3*, e03271.

Melaragno, J.E., Mehrotra, B., and Coleman, A.W. (1993). Relationship between endopolyploidy and cell size in epidermal tissue of Arabidopsis. Plant Cell *5*, 1661–1668.

Menges, M., de Jager, S.M., Gruissem, W., and Murray, J.A. (2005). Global analysis of the core cell cycle regulators of Arabidopsis identifies novel genes, reveals multiple and highly specific profiles of expression and provides a coherent model for plant cell cycle control. Plant J. *41*, 546–566.

Mi, H., Muruganujan, A., Ebert, D., Huang, X., and Thomas, P.D. (2019). PANTHER version 14: more genomes, a new PANTHER GO-slim and improvements in enrichment analysis tools. Nucleic Acids Res. *47*, D419–D426.

Morgan, D.O. (2007). The Cell Cycle : Principles of Control (New Science Press).

Nadeau, J.A., and Sack, F.D. (2002). Control of stomatal distribution on the Arabidopsis leaf surface. Science *296*, 1697–1700.

Nakagawa, T., Nakamura, S., Tanaka, K., Kawamukai, M., Suzuki, T., Nakamura, K., Kimura, T., and Ishiguro, S. (2008). Development of R4 gateway binary vectors (R4pGWB) enabling high-throughput promoter swapping for plant research. Biosci. Biotechnol. Biochem. *72*, 624–629.

Nakagawa, T., Suzuki, T., Murata, S., Nakamura, S., Hino, T., Maeo, K., Tabata, R., Kawai, T., Tanaka, K., Niwa, Y., et al. (2007). Improved Gateway binary vectors: high-performance vectors for creation of fusion constructs in transgenic analysis of plants. Biosci. Biotechnol. Biochem. *71*, 2095–2100.

Peres, A., Churchman, M.L., Hariharan, S., Himanen, K., Verkest, A., Vandepoele, K., Magyar, Z., Hatzfeld, Y., Van Der Schueren, E., Beemster, G.T., et al. (2007). Novel plant-specific cyclin-dependent kinase inhibitors induced by biotic and abiotic stresses. J. Biol. Chem. *282*, 25588–25596.

Peterson, K.M., and Torii, K.U. (2012). Long-term, high-resolution confocal time lapse imaging of Arabidopsis cotyledon epidermis during germination. J. Vis. Exp. *70*, 4426.

Pillitteri, L.J., Bogenschutz, N.L., and Torii, K.U. (2008). The bHLH protein, MUTE, controls differentiation of stomata and the hydathode pore in Arabidopsis. Plant Cell Physiol. *49*, 934–943.

Pillitteri, L.J., Peterson, K.M., Horst, R.J., and Torii, K.U. (2011). Molecular profiling of stomatal meristemoids reveals new component of asymmetric cell division and commonalities among stem cell populations in Arabidopsis. Plant Cell *23*, 3260–3275.

Pillitteri, L.J., Sloan, D.B., Bogenschutz, N.L., and Torii, K.U. (2007). Termination of asymmetric cell division and differentiation of stomata. Nature *445*, 501–505.

Putarjunan, A., Ruble, J., Srivastava, A., Zhao, C., Rychel, A.L., Hofstetter, A.K., Tang, X., Zhu, J.-K., Tama, F., Zheng, N., and Torii, K.U. (2019). Bipartite anchoring of SCREAM enforces stomatal initiation by coupling MAP kinases to SPEECHLESS. Nat. Plants *5*, 742–754.

Qi, X., Han, S.-K., Dang, J.H., Garrick, J.M., Ito, M., Hofstetter, A.K., and Torii, K.U. (2017). Autocrine regulation of stomatal differentiation potential by EPF1 and ERECTA-LIKE1 ligand-receptor signaling. Elife *6*, e24102.

Riou-Khamlichi, C., Huntley, R., Jacqmard, A., and Murray, J.A. (1999). Cytokinin activation of Arabidopsis cell division through a D-type cyclin. Science *283*, 1541–1544.

Robinson, J.T., Thorvaldsdóttir, H., Winckler, W., Guttman, M., Lander, E.S., Getz, G., and Mesirov, J.P. (2011). Integrative genomics viewer. Nat. Biotechnol. *29*, 24–26.

Roeder, A.H., Chickarmane, V., Cunha, A., Obara, B., Manjunath, B.S., and Meyerowitz, E.M. (2010). Variability in the control of cell division underlies sepal epidermal patterning in Arabidopsis thaliana. PLoS Biol. *8*, e1000367.

Sanz, L., Dewitte, W., Forzani, C., Patell, F., Nieuwland, J., Wen, B., Quelhas, P., De Jager, S., Titmus, C., Campilho, A., et al. (2011). The Arabidopsis D-type cyclin CYCD2;1 and the inhibitor ICK2/KRP2 modulate auxin-induced lateral root formation. Plant Cell *23*, 641–660.

Schindelin, J., Arganda-Carreras, I., Frise, E., Kaynig, V., Longair, M., Pietzsch, T., Preibisch, S., Rueden, C., Saalfeld, S., Schmid, B., et al. (2012). Fiji: an open-source platform for biological-image analysis. Nat. Methods *9*, 676–682.

Schwarz, E.M., and Roeder, A.H. (2016). Transcriptomic effects of the cell cycle regulator LGO in Arabidopsis Sepals. Front. Plant Sci. *7*, 1744.

Sherr, C.J., and Roberts, J.M. (2004). Living with or without cyclins and cyclin-dependent kinases. Genes Dev *18*, 2699–2711.

Sozzani, R., Cui, H., Moreno-Risueno, M.A., Busch, W., Van Norman, J.M., Vernoux, T., Brady, S.M., Dewitte, W., Murray, J.A., and Benfey, P.N. (2010). Spatiotemporal regulation of cell-cycle genes by SHORTROOT links patterning and growth. Nature *466*, 128–132.

Spitzer, M., Wildenhain, J., Rappsilber, J., and Tyers, M. (2014). BoxPlotR: a web tool for generation of box plots. Nat. Methods *11*, 121–122.

Stemmer, M., Thumberger, T., Del Sol Keyer, M., Wittbrodt, J., and Mateo, J.L. (2015). CCTop: an intuitive, flexible and reliable CRISPR/Cas9 target prediction tool. PLoS One *10*, e0124633.

Strzalka, W.K., Aggarwal, C., Krzeszowiec, W., Jakubowska, A., Sztatelman, O., and Banas, A.K. (2015). Arabidopsis PCNAs form complexes with selected D-type cyclins. Front. Plant Sci. *6*, 516.

Szklarczyk, D., Gable, A.L., Lyon, D., Junge, A., Wyder, S., Huerta-Cepas, J., Simonovic, M., Doncheva, N.T., Morris, J.H., Bork, P., et al. (2019). STRING v11: protein-protein association networks with increased coverage, supporting functional discovery in genome-wide experimental datasets. Nucleic Acids Res. *47*, D607–D613.

Tsutsui, H., and Higashiyama, T. (2017). pKAMA-ITACHI vectors for highly efficient CRISPR/Cas9-mediated gene knockout in Arabidopsis thaliana. Plant Cell Physiol. *58*, 46–56.

Van Leene, J., Hollunder, J., Eeckhout, D., Persiau, G., Van De Slijke, E., Stals, H., Van Isterdael, G., Verkest, A., Neirynck, S., Buffel, Y., et al. (2010). Targeted interactomics reveals a complex core cell cycle machinery in Arabidopsis thaliana. Mol. Syst. Biol. *6*, 397.

Vandepoele, K., Raes, J., De Veylder, L., Rouzé, P., Rombauts, S., and Inzé, D. (2002). Genome-wide analysis of core cell cycle genes in Arabidopsis. Plant Cell *14*, 903–916.

Vanneste, S., Coppens, F., Lee, E., Donner, T.J., Xie, Z., Van Isterdael, G., Dhondt, S., De Winter, F., De Rybel, B., Vuylsteke, M., et al. (2011). Developmental regulation of CYCA2s contributes to tissue-specific proliferation in Arabidopsis. EMBO J. *30*, 3430–3441.

Vatén, A., Soyars, C.L., Tarr, P.T., Nimchuk, Z.L., and Bergmann, D.C. (2018). Modulation of asymmetric division diversity through cytokinin and SPEECHLESS regulatory interactions in the Arabidopsis stomatal lineage. Dev. Cell *47*, 53–66.e5.

Walker, J.D., Oppenheimer, D.G., Concienne, J., and Larkin, J.C. (2000). SIAMESE, a gene controlling the endoreduplication cell cycle in Arabidopsis thaliana trichomes. Development *127*, 3931–3940.

Wang, K., Ndathe, R.W., Kumar, N., Zeringue, E.A., Kato, N., and Larkin, J.C. (2020). The CDK inhibitor SIAMESE targets both CDKA;1 and CDKB1 complexes to establish endoreplication in trichomes. Plant Physiol. *184*, 165–175.

Weimer, A.K., Matos, J.L., Sharma, N., Patell, F., Murray, J.A.H., Dewitte, W., and Bergmann, D.C. (2018). Lineage- and stage-specific expressed CYCD7;1 coordinates the single symmetric division that creates stomatal guard cells. Development *145*, dev160671.

Weimer, A.K., Nowack, M.K., Bouyer, D., Zhao, X., Harashima, H., Naseer, S., De Winter, F., Dissmeyer, N., Geldner, N., and Schnittger, A. (2012). Retinoblastoma related1 regulates asymmetric cell divisions in Arabidopsis. Plant Cell *24*, 4083–4095.

Wickham, H. (2016). ggplot2 : elegant graphics for data analysis. In Use R! (Springer), p. 1, online resource (XVI, 260 pages 232 illustrations, 140 illustrations in color.

Xie, Z., Lee, E., Lucas, J.R., Morohashi, K., Li, D., Murray, J.A., Sack, F.D., and Grotewold, E. (2010). Regulation of cell proliferation in the stomatal lineage by the Arabidopsis MYB four LIPS via direct targeting of core cell cycle genes. Plant Cell *22*, 2306–2321.

Zhang, Y., Guo, X., and Dong, J. (2016). Phosphorylation of the polarity protein BASL differentiates asymmetric cell fate through MAPKs and SPCH. Curr. Biol. *26*, 2957–2965.

Zhang, Y., Wang, P., Shao, W., Zhu, J.-K., and Dong, J. (2015). The BASL polarity protein controls a MAPK signaling feedback loop in asymmetric cell division. Dev. Cell *33*, 136–149.

Zhao, M.L., Rabiee, A., Kovary, K.M., Bahrami-Nejad, Z., Taylor, B., and Teruel, M.N. (2020). Molecular competition in G1 controls when cells simultaneously commit to terminally differentiate and exit the cell cycle. Cell Rep. *31*, 107769.

STAR★METHODS

KEY RESOURCES TABLE

Reagent or resource	Source	Identifier
Antibodies		
Anti-GFP antibody - ChIP Grade	Abcam	Abcam Cat. ab290, Lot. GR318425-1 RRID: AB_303395
Bacterial and virus strains		
Argrobacterium GV3101::pMP90	(Koncz et al., 1992)	n/a
Chemicals, peptides, and recombinant proteins		
Propidium iodide	Sigma-Aldrich	P4170
FM4-64	Invitrogen	T13320
DAPI	Sigma-Aldrich	D9542
cOmplete™, Mini Protease Inhibitor Cocktail	Roche	11836153001
β-Estradiol	Sigma-Aldrich	E2758
3-amino-1,2,4-triazole	Sigma-Aldrich	A8056
Deposited data		
Raw and processed MUTE ChIP-seq data	This study	GEO: GSE173338
iMUTE RNA-seq data	(Han et al., 2018)	GEO: GSE107018
iSPCH RNA-seq data	(Lau et al., 2014)	GEO: GSE57953
TAIR10 Arabidopsis annotation	TAIR	ftp://ftp.arabidopsis.org/home/tair/Genes/TAIR10_genome_release/
Experimental models: Organisms/strains		
Arabidopsis thaliana, Wild type (Col-0)	ABRC	CS1093
Arabidopsis thaliana, *mute*	(Pillitteri et al., 2007)	n/a
Arabidopsis thaliana, *mute-2*	(Pillitteri et al., 2008)	n/a
Arabidopsis thaliana, *iMUTE*	(Han et al., 2018)	n/a
Arabidopsis thaliana, *iSPCH*	(Han et al., 2018)	n/a
Arabidopsis thaliana, *proMUTE::MUTE-GFP scrm-D*	(Qi et al., 2017; Han et al., 2018)	n/a
Arabidopsis thaliana, *proSMR4::nucGFP (nls-3xGFP)*	This study	n/a
Arabidopsis thaliana, *proSMR4::nucGFP mute-2*	This study	n/a
Arabidopsis thaliana, *proSMR4::SMR4-YFP*	This study	n/a
Arabidopsis thaliana, *proSMR4::SMR4-YFP mute-2*	This study	n/a
Arabidopsis thaliana, *proSMR4::HA-SMR4 smr4-1cr*	This study	n/a
Arabidopsis thaliana, *smr4-1cr*	This study	n/a
Arabidopsis thaliana, *smr4-2cr*	This study	n/a
Arabidopsis thaliana, *smr8-1*	ABRC	SALK_126253
Arabidopsis thaliana, *smr8-2*	ABRC	SALK_074523
Arabidopsis thaliana, *smr4-1cr smr8-2*	This study	n/a
Arabidopsis thaliana, *proPOLAR::SMR4*	This study	n/a
Arabidopsis thaliana, *proPOLAR::SMR8*	This study	n/a
Arabidopsis thaliana, *proPOLAR::SMR1*	This study	n/a
Arabidopsis thaliana, *proPOLAR::KRP1*	This study	n/a
Arabidopsis thaliana, *proTMM::GUS-GFP*	ABRC (Nadeau and Sack, 2002)	CS65759

(*Continued on next page*)

Continued

Reagent or resource	Source	Identifier
Arabidopsis thaliana, *proPOLAR::SMR4 proTMM::GUS-GFP*	This study	n/a
Arabidopsis thaliana, *proMUTE::nucYFP*	(Qi et al., 2017)	n/a
Arabidopsis thaliana, *proPOLAR::SMR4 pMUTE::nucYFP*	This study	n/a
Arabidopsis thaliana, *E994*	ABRC (Pillitteri et al., 2007)	CS70070
Arabidopsis thaliana, *proPOLAR::SMR4 E994*	This study	n/a
Arabidopsis thaliana, *proSMR1::nlsGFP-GUS*	(Bhosale et al., 2018)	n/a
Arabidopsis thaliana, *proPOLAR::SMR4 proSMR1::nlsGFP-GUS*	This study	n/a
Arabidopsis thaliana, *PlaCCI*	(Desvoyes et al., 2020)	n/a
Arabidopsis thaliana, *LTI6b-GFP*	(Kurup et al., 2005) ABRC	CS84726
Arabidopsis thaliana, *PlaCCI Lti6b-GFP*	This study	n/a
Arabidopsis thaliana, *PlaCCI Lti6b-GFP proPOLAR::SMR4*	This study	n/a
Arabidopsis thaliana, *proPOLAR::SMR4 smr4-1cr*	This study	n/a
Arabidopsis thaliana, *proPOLAR::CYCD3;1*	This study	n/a
Arabidopsis thaliana, *proPOLAR::CYCD3;1 smr4-1cr*	This study	n/a
Arabidopsis thaliana, *proPOLAR::CYCD5;1*	This study	n/a
Arabidopsis thaliana, *proPOLAR::CYCD5;1 smr4-1cr*	This study	n/a
Arabidopsis thaliana, *proPOLAR::CYCD7;1*	This study	n/a
Arabidopsis thaliana, *proPOLAR::CYCD7;1 smr4-1cr*	This study	n/a
Arabidopsis thaliana, *proSMR4::HA-SMR4 smr4-1cr*	This study	n/a
Arabidopsis thaliana, *proPOLAR::SMR4 mute*	This study	n/a
Arabidopsis thaliana, *proRPS5a::H2B-GFP*	(Maruyama et al., 2013)	n/a
Arabidopsis thaliana, *proPOLAR::SMR4 proRPS5a::H2B-GFP*	This study	n/a
Saccharomyces cerevisiae (AH109 strain):	Clontech, (James et al., 1996)	n/a
AH109, *pGBKT7::SMR4*, *pGADT7*	This study	n/a
AH109, *pGBKT7::SMR4*, *pGADT7::CYCD3;1*	This study	n/a
AH109, *pGBKT7::SMR4*, *pGADT7::CYCD5;1*	This study	n/a
AH109, *pGBKT7::SMR4*, *pGADT7::CYCD7;1*	This study	n/a
AH109, *pGBKT7::SMR4*, *pGADT7::CDKA;1*	This study	n/a
AH109, *pGBKT7::SMR4*, *pGADT7::CDKB1;1*	This study	n/a
AH109, *pGBKT7*, *pGADT7::CYCD3;1*	This study	n/a
AH109, *pGBKT7*, *pGADT7::CYCD5;1*	This study	n/a
AH109, *pGBKT7*, *pGADT7::CYCD7;1*	This study	n/a
AH109, *pGBKT7*, *pGADT7::CDKA;1*	This study	n/a
AH109, *pGBKT7*, *pGADT7::CDKB1;1*	This study	n/a

(*Continued on next page*)

Continued

Reagent or resource	Source	Identifier
Oligonucleotides		
Plasmid construction	Table S3, this paper	n/a
Single guide RNA for *smr4* CRISPRing	Table S3, this paper	n/a
qRT-PCR primer/ genotyping	Table S3, this paper	n/a
Recombinant DNA		
pKI1.1R	(Tsutsui and Higashiyama, 2017)	Addgene #85808
pGWB440	(Nakagawa et al., 2007)	Addgene #74826
R4pGWB501	(Nakagawa et al., 2008)	n/a
Other recombinant DNAs generated in this study	Table S3, this paper	n/a
Software and algorithms		
Heatmapper	(Babicki et al., 2016)	http://www.heatmapper.ca/
CCTop - CRISPR/Cas9 target online predictor	(Stemmer et al., 2015)	https://cctop.cos.uni-heidelberg.de:8043/
R ver. 4.0.2	R Development Core Team, 2008	https://www.r-project.org/
R ggplot2 package	(Wickham, 2016)	n/a
BoxPlotR	(Spitzer et al., 2014)	http://shiny.chemgrid.org/boxplotr/
COLORBREWER 2.0	Penn State Univ.	http://www.ColorBrewer.org
FIJI-ImageJ	(Schindelin et al., 2012)	https://imagej.net/Fiji
Bowtie2	(Langmead and Salzberg, 2012)	http://bowtie-bio.sourceforge.net/bowtie2/index.shtml
Samtools	(Li et al., 2009)	http://samtools.sourceforge.net/
MACS (version 2.1.0.20140616)	(Feng et al., 2012)	http://liulab.dfci.harvard.edu/MACS
PANTHER	(Mi et al., 2019)	http://geneontology.org/
iGV	(Robinson et al., 2011)	https://software.broadinstitute.org/software/igv/
Other		
RNeasy Plant mini kit	Qiagen	74904
ACCEL-NGS® 2S PLUS DNA LIBRARY KIT with 2S Set A MID Indexing Kit	Swift bioscience	21024, 26148
ChIP DNA Clean & Concentrator	Zymo Research	D5205
ReverTra Ace™ qPCR RT Master Mix with gDNA Remover	TOYOBO	FSQ-301
KAPA SYBR® FAST for LightCycle® 480	KAPA Biosystems	KK4611
Dynabeads™ Protein G	invitrogen	1004D
SPRIselect	BECKMAN COULTER	B23317
NEBuilder® HiFi DNA Assembly Master Mix	NEB	E2621

RESOURCE AVAILABILITY

Lead contact

Further information and requests for resources and reagents should be directed and will be fulfilled by the Lead Contact, Keiko U. Torii (ktorii@utexas.edu).

Materials availability

Plasmids and transgenic plants generated in this study will be available from the lead contact upon request.

Data and code availability

- The ChIP-seq data generated in this study have been deposited at the NCBI Gene Expression Omnibus (GEO: GSE173338) and are publicly available. All data reported in this paper will be shared by the lead contact upon request.
- This paper does not report original code.

- Any additional information required to reanalyze the data reported in this paper is available from the lead contact upon request.

EXPERIMENTAL MODEL AND SUBJECT DETAILS

The Arabidopsis Columbia (Col) accession was used for wild type. The loss-of function mutants, complementation and reporter transgenic lines were reported listed in the key resources table. The T-DNA insertion mutants were obtained from the Arabidopsis Biological Resource Center (ABRC) at Ohio State Univ. CRISPR gene editing was performed to obtain SMR4 knock-out mutants. Transgenic lines were introduced into respective mutant backgrounds by genetic crosses or Agrobacterium (GV3101 pMP90 strain)-mediated transformation (see method details and key resources table for the lines generated) and genotypes were confirmed by PCR or Sanger sequencing. All recombinant DNAs for transgenes introduced to Arabidopsis are listed in Table S3. For sequence of genotyping primers, sequencing, and cloning see Table S3. Seedlings and plants were grown in a long-day or constant light condition at 22°C. For yeast two hybrid analysis, AH109 strain was used and resulting transformants were grown at 30°C.

METHOD DETAILS

Plasmid construction and generation of CRISPR-based mutant alleles

For a detailed information of constructs generated in this study, see Table S3. Primers used for plasmid constructs were listed in Table S3. For generation of transgenic Arabidopsis, plasmid constructs were electroporated into Agrobacterium (GV3101/pMP90) and subsequently transformed by floral dipping. Loss-of-function mutant of *SMR4* was generated by CRISPR by using pKAMA-ITACHI Vector (Addgene: 85808) as described previously (Tsutsui and Higashiyama, 2017). Briefly, primers for sgRNA were designed by the CCTop - CRISPR/Cas9 target online predictor (Stemmer et al., 2015). Primers were annealed and inserted into pKI1.1R vector cut with *AarI*. Resulting construct was introduced into wild-type Col-0 plants. T1 plants were screened by Hygromycin resistance. Six T1 lines were selected and sequenced to check whether mutations were introduced. One of the two sgRNAs was successful for generating mutations. In T2 generation, seeds that do not show OLE1-RFP signal were selected to exclude plants harboring transgene in the genome. We established two independent homozygous lines that contain 1 bp deletion (*smr4-1cr*) or 1 bp insertion *(smr4-2cr)* at *SMR4* gene (Figure S4). Primers used single guide RNA (sgRNA) for *SMR4* were listed in Table S3.

Plant growth condition and estradiol treatment

Arabidopsis accession Columbia (Col-0) was used as wild-type. The following mutants/transgenic lines are reported elsewhere: *mute-2* (Pillitteri et al., 2008); Lti6b (Kurup et al., 2005); PlaCCI (Desvoyes et al., 2020). T-DNA insertion mutants of *SMR8*, *smr8-1* (SALK_126253), *smr8-2* (SALK_074523) were obtained from ABRC. Their genotype and transcript reduction were confirmed. The following higher-order mutants/marker lines were generated by genetic crosses: *smr4-1cr smr8-1*, *proPOLAR*::*SMR4 mute-2*, *proSMR4*::*SMR4-YFP mute-2*, *proSMR4*::*nucGFP mute-2*, *PlaCCI Lti6b*, *proPOLAR*::*SMR4 PlaCCI*, and *smr4-1cr PlaCCI Lti6b*. The presence of transgenes/mutant alleles were confirmed by genotyping. All plant materials used in this study were listed in key resources table. Sterilized seeds were grown on half strength of Murashige and Skoog (MS) media with 1% sucrose at 22°C under continuous light and 10∼14-day-old seedlings grown on MS media were transplanted to soil to harvest seeds. For phenotyping of *smr* mutants, cotyledons at 4-day post germination stage were imaged. For phenotyping of transgenic plants of *proPOLAR*::*CKIs*, T2 plants were grown on ½ MS agar media containing hygromycin (15 μg/ml), and imaged at day 4 and day 8. For *proPOLAR*::*CYCD* transgenic plants, multiple independent T1 plants were selected from ½ MS agar media containing hygromycin (15 μg/ml) and imaged at day 7. For the complementation test of *SMR4*, T3 homozygous plants of *proSMR4*::*HA-SMR4* were germinated on ½ MS agar media were imaged at 5-day post germination (dpg).

Confocal microscopy

For confocal microscopy, cell peripheries of seedlings were visualized with either propidium iodide (Sigma, P4170) or FM4-64 (Invitrogen, T13320). Images were acquired using LSM800 (Zeiss) or SP5-WLL (Leica) using a 63x water lens. The Zeiss LSM800 was used to image the GFP and RFP reporter with excitation at 488 nm and an emission filter of 490 to 546 nm, and with excitation at 555 nm and 583-617 nm emission range, respectively. PlaCCI lines (Desvoyes et al., 2020) were imaged using SP5-WLL with the following conditions: CFP, excitation at 458 nm and emission from 468 to 600 nm; GFP, excitation at 488 nm and emission from 490 to 546 nm; YFP, excitation at 514 nm and emission from 524 to 650 nm; mCherry, excitation at 560 nm and emission from 590 to 650 nm. Signals were visualized sequentially using separate HyD detectors. DIC images were taken to delineate the cell outlines (shown in magenta). Raw data were collected with 1024 x 1024 pixel image and imported into Fiji-ImageJ to generate CYMK images using the channel merge function. The time-lapse were collected at 30-min intervals using a 20x lens (Peterson and Torii, 2012; Qi et al., 2017). Raw images were imported into Fiji-ImageJ to generate time projections using the Stacks function. For higher quality time-lapse imaging of PlaCCI x LTi6b lines in different genetic backgrounds, we used Leica Stellaris 8 FALCON with the following conditions: CFP, excitation at 458 nm and emission from 464 to 510 nm; YFP excitation at 514 nm and emission from 520 to 560 nm; mCherry, excitation at 561 nm and emission from 570 to 620 nm. Signals were visualized sequentially using separate HyD detectors (HyDX/HyDS) in TauSeparation mode. The time-lapses were collected at 30-min intervals using a 63x oil-lens, zoom

factor 1.5. Raw data were collected with 512 x 512 pixel image and imported into Fiji-ImageJ v1.8.0_66 to generate RGB images/z-stacks using the channel merge function. To correct for drift of multichannel z-stacks the "StackReg" plugin was applied.

Quantitative analysis of epidermal phenotype

For quantitative analysis of abaxial leaf epidermis of *smr* mutants and transgenic plants, confocal images were taken at the days after germination as indicated in the Figure legends. Preparation of images was done as described previously (Houbaert et al., 2018). For counting epidermal cell types, stomatal density, stomatal precursor cells (meristemoids and GMC), total epidermal cells (stomata, meristemoids, GMC and pavement cells) and stomata index (number of stomata / number of total epidermal cells x100) were calculated by counting cell types in an area of 0.45 mm^2 (0.67 mm x 0.67 mm) at the developmental stage indicated with the cell counter plug-in in Fiji, and plotted as per mm^2. The epidermal cell areas of *smr* mutants were color-coded-coded depending on the area calculated using ROI_Color_Coder with a range of min-max (0-4000) in Fiji. The epidermal cells were subdivided into 9 groups according to their size. One representative image from each genotype was analyzed and the cell size distribution was then calculated from 499 cells for Col-0 plants, 659 cells for *smr4-1*, 662 cells for *smr4-2*, 601 cells form *smr8-1*, 611 cells form *smr8-1* and 755 cells for *smr4-1cr smr8-1* double mutant. Guard cells were excluded for the cell size measurement.

For cell size and circularity measurement of stomatal lineage precursors, images of *proTMM*::*GUS-GFP* were set to grayscale and GFP expressing cells were colored in black while other cell area in white by photoshop, then the images were imported to Fiji. Imported images were subjected to Images > Threshold; Analyze > analyze particle. Shape descriptors box has to be checked in "Set measurement" under the Analyze tab to get circularity values from the selected cell area. For the meristemoid size in *mute* mutant background was measured by the same methods.

cDNA preparation and qRT-PCR

For chemical treatment, plants were grown on media containing either 10uM β-estradiol (Sigma, E8875) or DMSO. For time-course induction, estradiol-inducible MUTE or SPCH seeds were sown on 1/2 MS media, and subjected to stratification at 4°C for two to three days then grown for the four to five days under continuous light. Subsequent steps were performed as described Han et al. (2018) (Han et al., 2018). RNA was isolated using RNeasy Plant Mini Kit (Qiagen, 74904). 0.5 μg of RNA was converted to cDNA using ReverTra Ace™ qPCR RT Master Mix with gDNA Remover (TOYOBO, FSQ-301) according to the instructions of the manufacturer. qRT-PCR was performed as described in Han et al. (2018) (Han et al., 2018) using KAPA SYBR® FAST qPCR Kit Master Mix on LightCycler® 96 instrument (Roche). Relative expression was calculated by dividing *ACTIN2* gene expression over the specific-gene expression and the fold change was calculated by dividing estradiol expression over DMSO (mock) expression at each time point indicated. See Table S3 for primer sequences used for qRT-PCR.

Chromatin immunoprecipitation sequencing (ChIP-seq)

For MUTE ChIP-seq experiments, transgenic plants *proMUTE*::*MUTE-GFP scrm-D* were prepared as described previously (Han et al., 2018) with following modifications. To shear the DNA, Bioruptor (Diagnode) was used, 30 sec on and 30 sec off cycle 15∼18 times. Immunoprecipitation against GFP was performed using anti-GFP antibody (Abcam, ab290, Lot. GR318425-1). DNAs from the immuno-complex was purified by kit (Zymo Research, D5205). The half of the purified DNA was subjected to library preparation using ACCEL-NGS® 2S PLUS DNA LIBRARY KIT with 2S Set A MID Indexing Kit (Swift bioscience, 21024, 26148) for next generation sequencing. Quantitative PCR (qPCR) was carried out using gene specific primers (Table S3) to confirm the library construction. The qPCR was run using KAPA SYBR® FAST qPCR Kit Master Mix on LightCycler® 96 instrument (Roche) as previously described (Han et al., 2018). Three biological replicates were used for MUTE ChIP-seq experiments. Size distribution of the libraries was validated by 2100 Bioanalyzer (Agilent). The prepared libraries (Col input and IP, MUTE-GFP input and IP with three replicates) were sequenced 35 bp paired-end in length with 30million coverage per sample on Illumina NextSeq 500 system. ChIP mapping and peak calling were performed as described in Feng et al. (2012) (Feng et al., 2012). Output reads were mapped to the TAIR10 genome assembly using bowtie2 and resulting bam files were sorted and indexed via samtool. The sorted bam files were subjected for MACS peak calling (version 2.1.0.20140616) (Table S2). Bedgraph file was generated and visualized in igv browser. Gene Ontology enrichment analysis was performed using GENE ONTOLOGY (http://geneontology.org/) combined with manual curation to remove redundant terms. Genes increased by MUTE more than Log_2 FC (Fold Change) 0.4 and targeted by MUTE were tested (Table S2). Following multiple hypothesis testing correction (Bonferroni-correction), GO term with FDR <0.05 were called significantly enriched (Table S2). The ChIP-seq data generated in this study are deposited to the NCBI with an accession number GEO: GSE173338.

Measurement of DNA content and nuclei size

1st true leaves were harvested from 16-day old plants and fixed in a solution of 9:1 (v/v) ethanol: acetic acid for overnight. For DAPI staining, tissues were rehydrated with ethanol series. DAPI (4'6-diamidino-2'-phenylindole) staining was done in 5μg/ml final concentration for 15 minutes in dark. Nuclear DAPI fluorescence was excited at 405 nm captured with 410 -470 nm emission range. DAPI stained nuclei area from the guard cells was selected and measured by using FIJI software. Wild-type and two independent T2 *proPOLAR*::*SMR4* transgenic lines were used. The number of guard cells measured is 129 (WT) and 234 (*proPOLAR*::*SMR4*). 10 or 11-day-old cotyledons from *proRPS5A*::*H2B-GFP* (Maruyama et al., 2013) transgenic plants were also imaged to measure the nuclei size of guard- and pavement cells. The area of nuclei (GFP) was selected and measured from the z-stack

projection images using FIJI software. Number of guard cells and pavement cells measured; 155 and 108 (wild type), 191 and 103 (*proPOLAR*::*SMR4 proRPS5A*::*H2B-GFP*). DAPI-stained nuclear area of single-celled GCs in *proPOLAR::SMR1* (n = 24) and normal GCs in wild type (n = 102) in 12-day old true leaves was measured.

Yeast two hybrid assay

Y2H assays were performed using the Matchmaker™ Two-Hybrid System (Clontech). Bait (pGBKT7) and prey (pGADT7) constructs were co-transformed into the yeast strain AH109 according to manufactural instruction (Clontech). The resulting transformants were spotted on SD (−Leu, −Trp) and SD (−Trp, −Leu, −His) selection media containing different concentration of 3-amino-1,2,4-triazole (Sigma, A8056) as previously reported (Putarjunan et al., 2019). All constructs and primer information are listed in the Table S3.

QUANTIFICATION AND STATISTICAL ANALYSIS

A series of Z-stack confocal images were taken to obtain images covering the epidermis and capturing GFP signal from the reporter lines. The area and the number of epidermal cells were quantified by using FIJI-ImageJ. Statistical analyses were performed using R ver. 4.0.2. For the multiple sample comparison, one-way ANOVA with post-hoc Tukey HSD test was performed. For the two-sample comparison, either student t-test or Mann-Whitney U test were performed. Graphs were generated using R ggplot2 package, BoxPlotR or Microsoft Excel (Listed in key resources table). The color of Boxplot graph was based on ColorBrewer.org. The value of n, the number of each experiment or samples, means of error bars, and how statistical significance was defined are indicated in a relevant figure legend.

Developmental Cell, Volume *57*

Supplemental information

Deceleration of the cell cycle underpins a switch from proliferative to terminal divisions in plant stomatal lineage

Soon-Ki Han, Arvid Herrmann, Jiyuan Yang, Rie Iwasaki, Tomoaki Sakamoto, Bénédicte Desvoyes, Seisuke Kimura, Crisanto Gutierrez, Eun-Deok Kim, and Keiko U. Torii

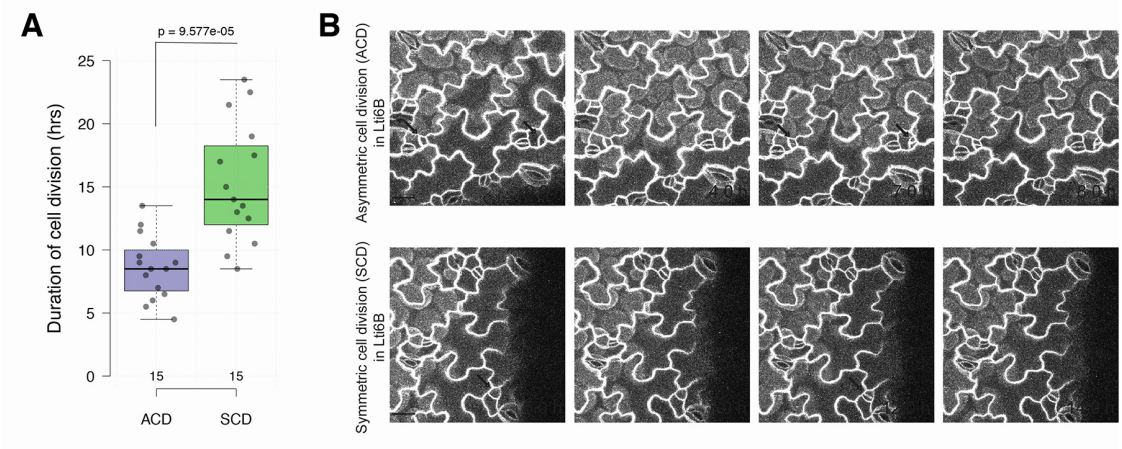

Figure S1. Cell division time of amplifying ACD is faster than that of the terminal SCD, Related to Figure 1

(A) Duration of the division time of stomatal precursors undergoing ACD and SCD measured by plasma membrane marker Lti6B line. n=15 for each cell division mode. Two-tailed Student t-test was performed. p=9.577 e-05.

(B) Still images series of representative ACD and SCD duration in plasma membrane marker Lti6B line. Black arrows indicate the meristemoid in amplifying ACD (top) or GMC undergoing SCD (bottom), respectively. Scale Bar: 20 μm

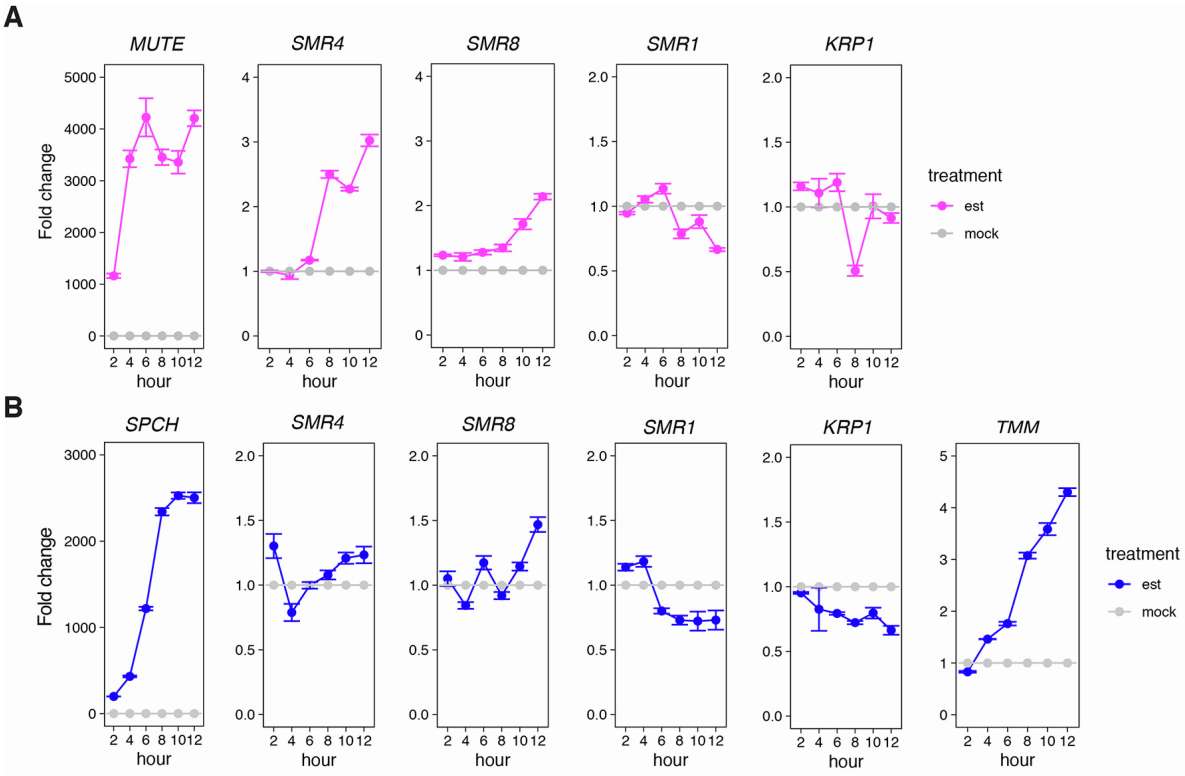

Figure S2. Time course analysis of *SMRs* and *KRP1* expression fold change upon induction of MUTE and SPCH, Related to Figure 2

(A, B) Representative qRT-PCR analysis of SMRs and KRP1 expression fold change upon MUTE induction (A) and SPCH induction (B) by estradiol application. In both cases, qRT-PCR was normalized against *ACT2,* and then expression fold change upon MUTE/SPCH induction was normalized against mock control at each time point. Bars, mean of three technical replicates. Error bars, mean ± s.e.m. Mock: DMSO only, est: 10 μM estradiol

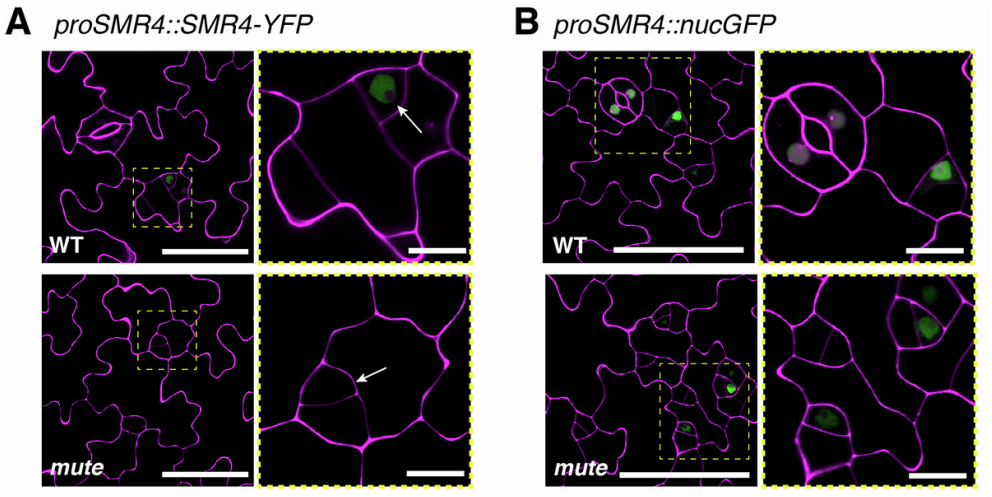

Figure S3. SMR4 transcriptional and translational reporter expressions in *mute*, Related to Figure 2

(A) Confocal microscopy images of cotyledon abaxial epidermis from 5-day-old Arabidopsis wild-type (top) and *mute-2* (bottom) seedlings expressing *proSMR4::SMR4-YFP*. In wild type, SMR4-YFP signal (green) is visible in the nucleus of a late meristemoid (arrow). No SMR4-YFP signal is observed in *mute-2* late meristemoid (arrow). Yellow dotted areas in the left panels are enlarged in the right panels. Scale bars, 50 μm (left panels), 10 μm (right panels).

(B) Confocal microscopy images of cotyledon abaxial epidermis from 5-day-old Arabidopsis wild-type (top) and *mute-2* (bottom) seedlings expressing *proSMR4::nucGFP*. In wild type, nucGFP signal (green) is visible in a late meristemoid to immature guard cells (some residual GFP signals are visible in guard cells). In *mute-2,* weak, background GFP signals can be detected in some meristemoids and SLGCs, implying general expression of SMR4. Yellow dotted areas in the left panels are enlarged in the right panels. Scale bars, 50 μm (left panels), 10 μm (right panels).

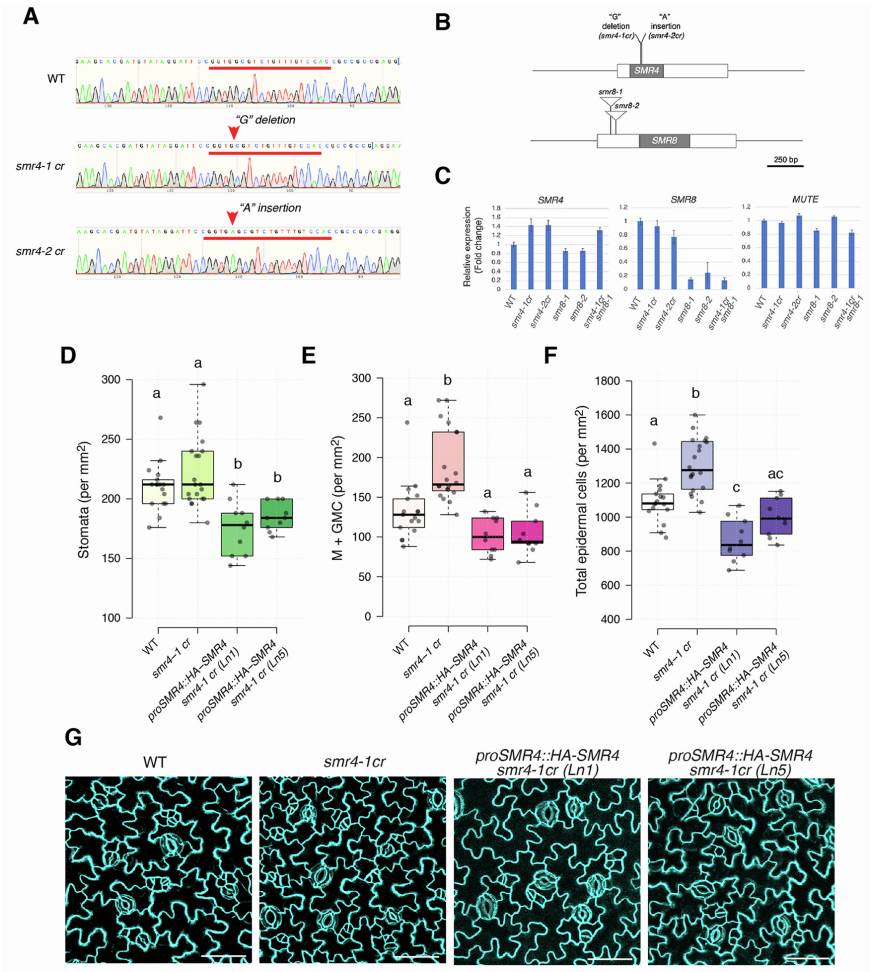

Figure S4. Characterization of *smr4 and smr8* mutants and complementation test, Related to Figure 3

(A) Comparison of Sanger sequencing chromatograms of WT and two homozygous CRISPR mutant alleles of *SMR4*, *smr4-1cr* and *smr4-2cr*, indicating the exact location of 1-base deletion (G deletion) and insertion (A insertion), respectively. (B) Location of mutation introduced at *SMR4 CRISPR* and *SMR8 T-DNA* loci. Two *smr8* mutants (*smr8-1*: SALK_126253 and *smr8-2*: SALK_074523) have T-DNA inserted at 5' UTR. Gray, exon; white, 5' and 3' UTR.

(C) qRT-PCR analysis of relative *SMR4* and *SMR8* expression in each single mutant and a double mutant. The transcripts were normalized against *ACT2* first, then plotted relative to transcript levels in wild-type seedlings. *MUTE* was used as a negative control. Error bars, mean ± s.e.m from three technical replicates. Ridges inside GCs can be seen due to z-stack images.

(D-G) Complementation analysis. *proSMR4::HA-SMR4* is introduced into *smr-4-1cr* mutant plants. Cotyledons from two independent lines harboring homozygous transgenes were imaged at the 5 -day post germination and the number of epidermal cells were counted. Number of stomata (D), number of stomatal precursor cells (E), and number of epidermal cells (F) per 1.0 mm^2. One-way ANOVA followed by Tukey's HSD analysis indicates that *scr4-1cr* epidermal/stomatal phenotypes are fully rescued. WT: n=17, *smr4-1cr*: n=20, Complementation Ln1: n=10, and Ln5: n=10 (G) Confocal microscopy images of 5-day-old cotyledon abaxial epidermis from wild-type (WT), *smr4-1cr*, *proSMR4::HA-SMR4 smr4-1cr* Line 1, and Line 5, showing full complementation.

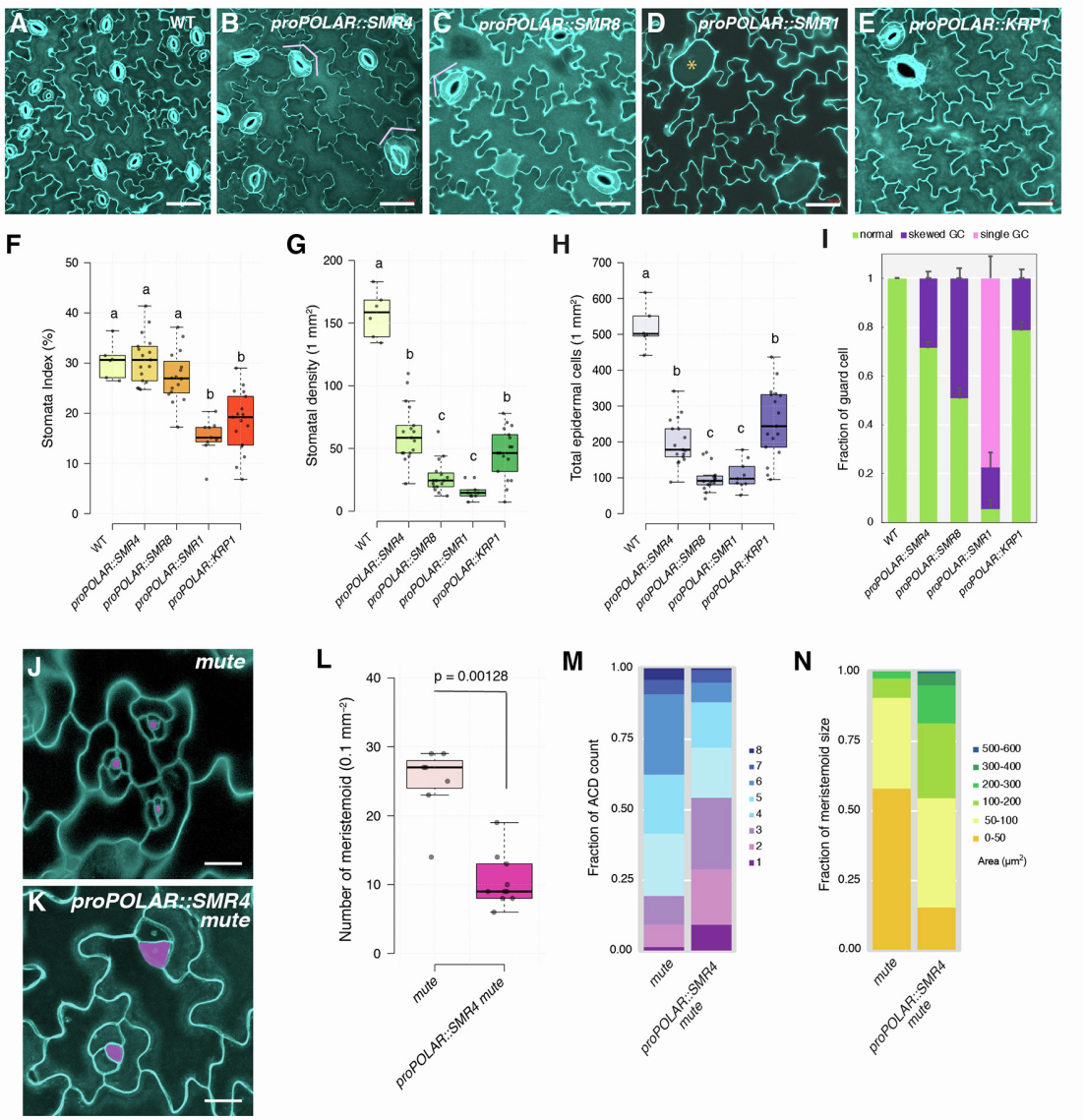

Figure S5. SMRs and KRP1 display distinct activity in epidermal cell development, Related to Figure 4

(A-E) Epidermal phenotype of 8 dpg abaxial cotyledon from WT (A), *SMR4* (B), *SMR8* (C), *SMR1* (D) and *KRP1* (E) driven by the *POLAR* promoter. Scale bar: 50 μm. (F-I) Stomatal index (F), stomatal density (G), total epidermal number (H), and fraction of normal, skewed and single-celled stomata (I) in the unit area per mm^2. Error bars, SD

(J) *mute* mutant, (K) *proPOLAR::SMR4* introduced into *mute*, images were taken at 2-week old cotyledons. Arrested meristemoids are false colored in magenta. (L) The number of meristemoids per 0.1 mm^2 area (*mute*: n=7, *proPOLAR::SMR4 mute*: n= 9). (M) The fraction of the ACD count, (N) Size distribution of meristemoid, 86 and 204 meristemoids were used for *mute* and *proPOLAR::SMR4 mute*, respectively.

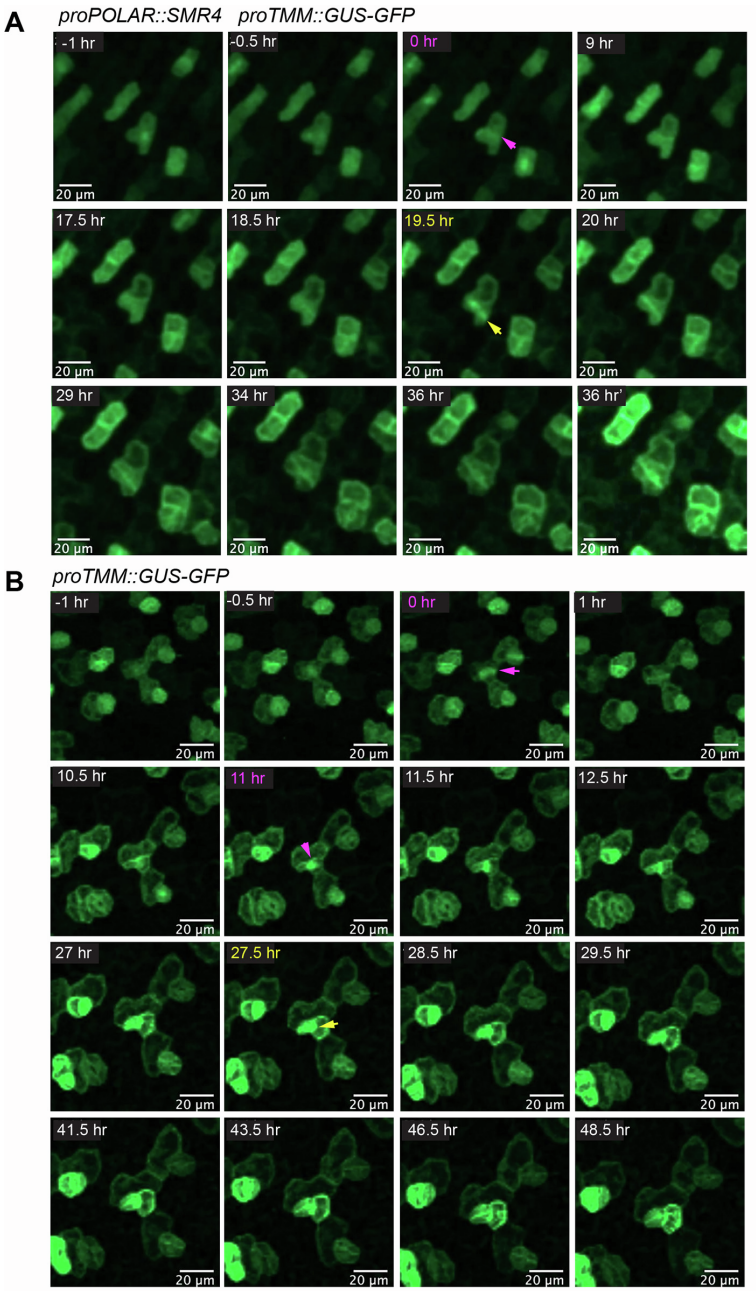

Figure S6: Time-lapse imaging of *proTMM::GUS-GFP* epidermis highlights the effects of *proPOLAR::SMR4* on delayed and aberrant ACDs, Related to Figure 5, Movies S7 and S8
Shown are still images from time-lapse live imaging of *proTMM::GUS-GFP* in *proPOLAR::SMR4* (A) and wild type (B). A magenta and yellow arrow indicate ACD and SCD division plane, respectively. Hours are displayed relative to the time when ACD plane is first visible and indicated at the left top corner. Scale bars, 20 µm

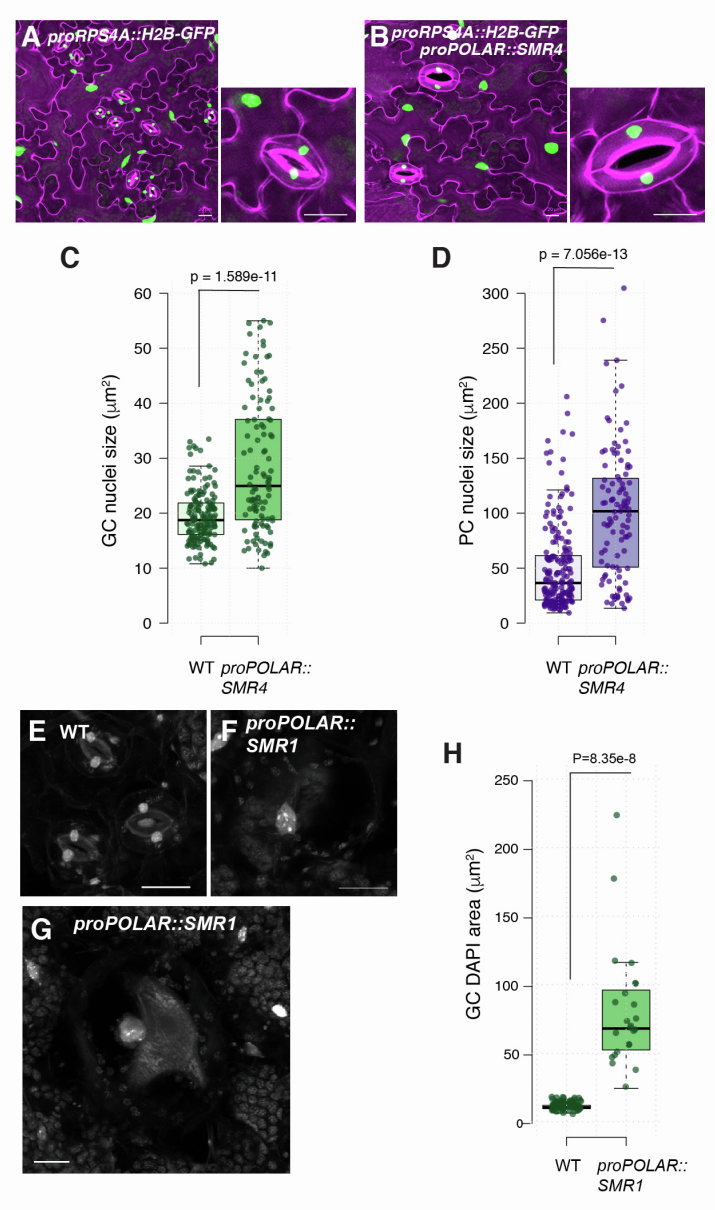

Figure S7. SMR4 does not trigger endoreduplication unlike SMR1, Related to Figure 5
(A-B) Orthogonal projection image from z-stack images covering whole nuclei from epidermis (A) *proRPS5A::H2B-GFP*, (B) *proRPS5A::H2B-GFP proPOLAR::SMR4,* Insets: mature guard cells, Scale bars: 20 µm. (C) Measurement of guard cell (GC) nuclei size, The area of 155 and 108 GC nuclei from wild type and *proPOLAR::SMR4*, respectively were measured. Student t-test was performed ($P<1.58911e^{-11}$). (D) Measurement of pavement cell (PC) nuclei size. The area of PC was measured. n= 191 (wild type), n=103 (*proPOLAR::SMR4*). Student t-test was performed ($P< 7.05614e^{-13}$). (E-G) DAPI stained nuclei in wild type (E) and single-celled stomata from *proPOLAR::SMR1* (F,G), Scale bar, 20 µm. (H) Quantitative analysis of DAPI-stained nuclear area in wild-type mature GC (n=102) and *proPOLAR::SMR1* (n=24) single-celled GCs. Two-tailed Student t-test was performed. p=8.35e-8.